

First Observations of Beam Spin Asymmetries for K⁺

David M. Riser

June 2018

Contents

1	Introduction	5
2	Experiment	9
2.1	CEBAF	9
2.1.1	Electron Injection & Polarization	9
2.1.2	Acceleration of Electrons	11
2.2	CLAS in Jefferson Lab Experimental Hall B	13
2.2.1	CLAS Torus and Drift Chambers	14
2.2.2	CLAS Cherenkov Counter	15
2.2.3	CLAS Time of Flight Scintillator	15
2.2.4	CLAS Electromagnetic Calorimeter	16
2.2.5	E1-F	17
3	Basic Analysis & Corrections	19
3.1	Introduction	19
3.2	Determination of Good Run List	19
3.3	Helicity Determination	19
3.4	Vertex Corrections	20
3.5	Timing Corrections	20
3.6	Kinematic Corrections	22
4	Particle Identification	27
4.1	Introduction	27
4.2	Electron Identification	27
4.2.1	Electron ID Cuts	27
4.3	Hadron Identification	38
4.3.1	Hadron ID Cuts	38

5 Beam Spin Asymmetry Analysis	47
5.1 Introduction	47
5.2 Event Selection and Binning	47
5.3 ϕ_h Distributions	50
5.4 Extraction of Modulations	56
References	63

Chapter 1

Introduction

Protons and neutrons (nucleons) are spin-half fermions. Exactly how quarks and gluons dynamically combine to produce the net spin-half of the nucleon is not clear. Striking results of g_2 measurements performed by the European Muon Collaboration (EMC) in 1988 [1] demonstrated that only 30% of the spin of the nucleons can be attributed to quark spin. This result became known as the *proton spin crisis*, and remains largely unresolved. The understanding of quark orbital angular momentum in the nucleon, and it's contribution to the proton spin, is of vital importance.

Addressing the question of orbital angular momentum distributions of partons within nucleons motivates moving beyond a co-linear picture of parton interactions. During the early 1990s, theoretical tools began to emerge that are now being used to study quark dynamics in three-dimensions. Transverse momentum dependent functions (TMDs) naturally extend the co-linear parton distribution functions (PDFs) to include intrinsic quark momentum in the plane transverse to the hard probe [2, 3].

Sadly, TMDs are not directly observable. Despite this fact, single spin asymmetry (SSA) measurements of semi-inclusive deeply inelastic scattering (SIDIS) have proven useful in recent years as inputs for phenomenological extraction of TMD parton distribution functions (TMD PDFs, sometimes just called TMDs) and TMD fragmentation functions (TMD FFs or simply FFs) [4–6]. Because of the absence of a TMD PDF, semi-inclusive annihilation of $e^+e^- \rightarrow h_1h_2X$ has been successfully used as input to TMD FF extractions [7].

By assuming single photon exchange and writing the QED interaction between the virtual photon and the nucleon as a generic vertex, then applying hermiticity, parity, and naive time-reversal invariance, the cross section for SIDIS can be written in a model independent way in terms of structure functions [2, 3].

$$\frac{d^5\sigma}{dx_B dQ^2 dz d\phi_h dp_{h\perp}^2} = \frac{\alpha_{em}^2}{2x_B y Q^2} \frac{y^2}{1-\varepsilon} \left(1 + \frac{\gamma^2}{2x_B}\right) \left\{ F_{UU,T} + \varepsilon F_{UU,L} \right. \\ \left. + \sqrt{2\varepsilon(1+\varepsilon)} \cos\phi_h F_{UU}^{\cos\phi_h} + \varepsilon \cos(2\phi_h) F_{UU}^{\cos 2\phi_h} + \lambda_e \sqrt{2\varepsilon(1-\varepsilon)} \sin\phi_h F_{LU}^{\sin\phi_h} \right\} \quad (1.1)$$

Here, typical definitions for the SIDIS kinematic variables are used (where $q = l - l'$ and $Q^2 = -q^2$).

$$x = \frac{Q^2}{2P \cdot q} \quad y = \frac{P \cdot q}{P \cdot l} \quad z = \frac{P \cdot P_h}{P \cdot q} \quad \gamma = \frac{2Mx}{Q} \quad (1.2)$$

Additionally, the ratio ε of the longitudinal and transverse photon flux is shown below.

$$\varepsilon = \frac{1 - y - \frac{1}{4}\gamma^2 y^2}{1 - y + \frac{1}{2}y^2 + \frac{1}{4}\gamma^2 y^2} \quad (1.3)$$

The factor λ appearing in the cross section refers to the helicity state of the incoming lepton, and ϕ_h is the angle between the lepton and hadron scattering planes. By measuring the cross section for both electron helicity states, the beam spin asymmetry can be constructed.

$$BSA = \frac{d\sigma^+ - d\sigma^-}{d\sigma^+ + d\sigma^-} = \frac{A_{LU}^{\sin\phi_h} \sin\phi_h}{1 + A_{UU}^{\cos\phi_h} \cos\phi_h + A_{UU}^{\cos(2\phi_h)} \cos(2\phi_h)} \quad (1.4)$$

Where the coefficient $A_{LU}^{\sin\phi}$ is defined as,

$$A_{LU}^{\sin\phi_h} = \sqrt{2\varepsilon(1-\varepsilon)} \frac{F_{LU}^{\sin\phi_h}}{F_{UU,T} + \varepsilon F_{UU,L}} \quad (1.5)$$

and the unpolarized moments are defined in a similar way. Within the TMD framework, the structure function $F_{LU}^{\sin\phi_h}$ is a pure twist-three structure function. With the assumption of twist-three factorization (which has not been demonstrated) the structure function is composed of four terms.

$$F_{LU}^{\sin\phi_h} = \frac{2M}{Q} \mathcal{C} \left[-\frac{\hat{\mathbf{h}} \cdot \mathbf{k}_T}{M_h} \left(xeH_1^\perp + \frac{M_h}{M} f_1 \frac{\tilde{G}^\perp}{z} \right) + \frac{\hat{\mathbf{h}} \cdot \mathbf{p}_T}{M} \left(xg^\perp D_1 + \frac{M_h}{M} h_1^\perp \frac{\tilde{E}}{z} \right) \right] \quad (1.6)$$

The notation \mathcal{C} is shorthand presented in [3] as a way to write structure functions in terms of the convolutions of PDF and FF objects.

$$\mathcal{C}[\omega fD] = x \sum_a e_a^2 \int d^2\mathbf{p}_T d^2\mathbf{k}_T \delta^{(2)}(z\mathbf{k}_T + \mathbf{p}_T - \mathbf{P}_{h\perp}) \omega(\mathbf{k}_T, \mathbf{p}_T) f^a(x, k_T^2) D^a(z, p_T^2) \quad (1.7)$$

Here the summation over quark flavors a is explicitly shown.

At twist-three four TMD PDFs appear in the structure function, one of which is known as the Boer-Mulders function h_1^\perp . The Boer Mulders TMD is a twist-two time-reversal odd function. Additionally,

g^\perp is a twist-three time reversal odd TMD, that has been compared to a higher twist analog of the Sivers function. Finally, e is a chiral odd twist-three TMD and f_1 the unpolarized TMD. Two twist-three fragmentation functions appear in the expression \tilde{G}^\perp , \tilde{E} , as the leading twist Collins H_1^\perp and D_1 the fragmentation functions.

Despite measurements of $A_{LU}^{\sin\phi_h}$ for π^+ , π^- , and the neutral π^0 mesons [8], little is known about the contribution of each individual PDF/FF term to the asymmetry. Still fewer are the SSA measurements which have tagged kaons in the final state. Previous analyses have reported results for the Sivers asymmetry $A_{UT}^{\sin(\phi_h - \phi_S)}$, which was recently reported by Hall A [9] and was observed with a small magnitude. However, measurements by the HERMES collaboration indicate that the Sivers asymmetry has quite a large magnitude [4].

This measurement of K^+ beam spin asymmetries is not consistent with zero, and further provides evidence that at the presently studied kinematics, intrinsically twist-three distributions functions are not vanishingly small.

Chapter 2

Experiment

Jefferson National Lab houses the continuous electron beam accelerator facility (CEBAF) which is currently capable of providing 11 GeV electron beams to three experimental end stations, and 12 GeV to a fourth. The data that are analyzed in this study are from the run period E1-F, which occurred before the 12 GeV CEBAF upgrade, the details in this chapter describe the accelerator and CLAS detector at the time of the E1-F run period.

2.1 CEBAF

Proposed in 1982 and constructed between 1987-1997 the CEBAF accelerator at Jefferson lab was composed of a pair of linear accelerators and 9 recirculating arcs arranged in a racetrack shape [10, 11]. Originally designed to provide 4 GeV unpolarized electrons to three experimental halls, CEBAF was fitted with twin polarized electron guns, and upgraded to 6 GeV beam energy before the E1-F run period. CEBAF was built to provide an extremely high duty factor and an average beam current of up to $200 \mu A$.

2.1.1 Electron Injection & Polarization

CEBAF's injector provided 45 MeV electrons with 70%-80% longitudinal polarization for the main accelerator. In order to provide an apparent continuous stream of events to the detectors, electron bunches were produced at a rate of $f = 1497 \text{ Mhz}$. To accommodate different requests for energy and beam current simultaneously, the injector produced three interspersed bunch trains at a frequency of 499 Mhz . The output injector energy $E = 45 \text{ MeV}$ was chosen so that injected electrons were *sufficiently relativistic*. In other words, when bunches of electrons at different energies simultaneously passed through the

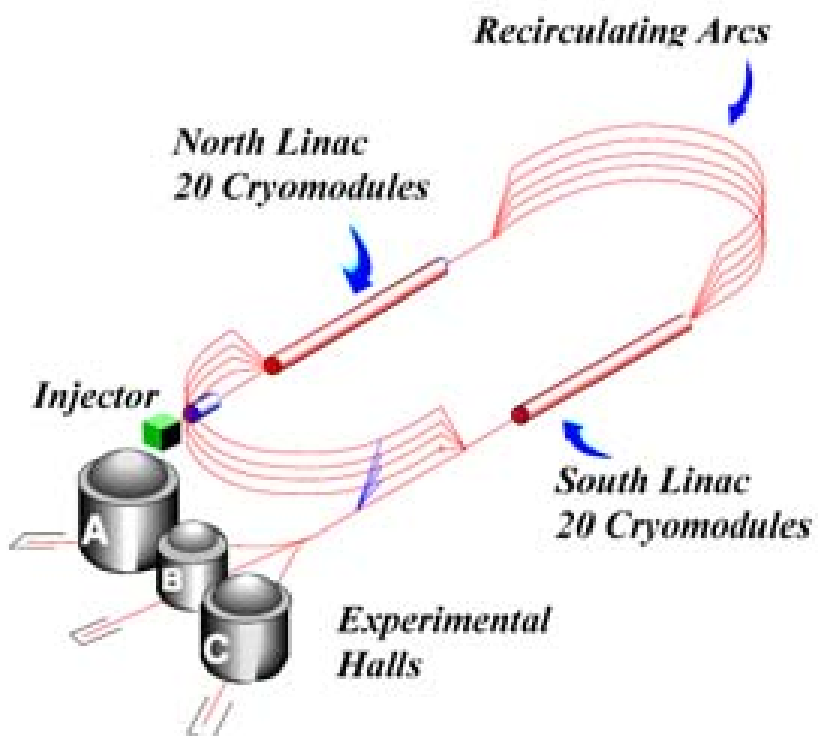


Figure 1: Layout of CEBAF.

Figure 2.1: Diagrammatic representation of CEBAF.

linear accelerators (LINACs), the relative phase difference (between different energy passes) accumulated over the distance remained less than 1° .

During early accelerator construction, the need for polarized electrons became apparent and the final polarized electron gun was produced in 2000. Production of polarized electrons was achieved by using twin polarized electron guns mounted at 15° with respect to the injector beam axis. Inside of each gun, electrons were liberated from gallium arsenide photo-cathodes by three independent diode lasers operated at a repetition rate of 499 Mhz . During polarized production, the diodes operated at a central wavelength of 850 nm . By manipulating the laser polarization using a Pockels cell, the electron beam spin is flipped at a rate of 60 Hz . Throughout the run period, an overall phase difference could be introduced by rotation of a wave-plate. As will be discussed in some detail later, changes in beam helicity due to wave-plate settings must be removed from the recorded data. After acceleration to 5 MeV the beam polarization was measured in the injector facility using a Mott polarimeter.

2.1.2 Acceleration of Electrons

The north and south LINACs were responsible for increasing the energy of the electrons from 45 MeV up to an impressive $\approx 5.7\text{ GeV}$ before delivery to the experimental halls A, B, and C. In order to achieve this each bunch of electrons was accelerated through ten stages, five passes through each LINAC. The strong electric field needed to accelerate electron bunches was confined inside of superconducting 5-cell elliptical cavities. These cavities were machined from niobium, and operated at a temperature of 2.2° K . Developed at Cornell University, the cavities were operated at $1,500\text{ Mhz}$ with a gradient greater than 5 MV/m and a quality factor $Q_0 \geq 3 \cdot 10^9$ (the Q factor describes the monochromaticity of the cavity and is defined $Q_0 = f_0/\Delta f$). Each cavity was sealed inside of a cryo-unit, four such units were connected together to form an 8.5 meter cryo-module. Each LINAC was composed of 20 such cryo-modules connected together to increase electron energies by more than 500 MeV per pass.

The radio frequency (RF) that powers each cavity was sourced by a water-cooled 5 kilowatt Klystron located in groups of eight above each cryo-module. Phase locking of each cavity with a master oscillator ensured that the difference in phase between all cavities was less than one degree. The important super conductivity was maintained by circulation of liquid helium at 2.2° K . Production of liquid helium occurred on-site at the 5 kW helium liquefaction plant.

After re-circulation of five passes through each LINAC, full energy beams were delivered to the halls. Bunches were separated using an RF separator before entering their respective experimental



Figure 2.2: This aerial photograph contains annotations that show the accelerator path and the three experimental halls.

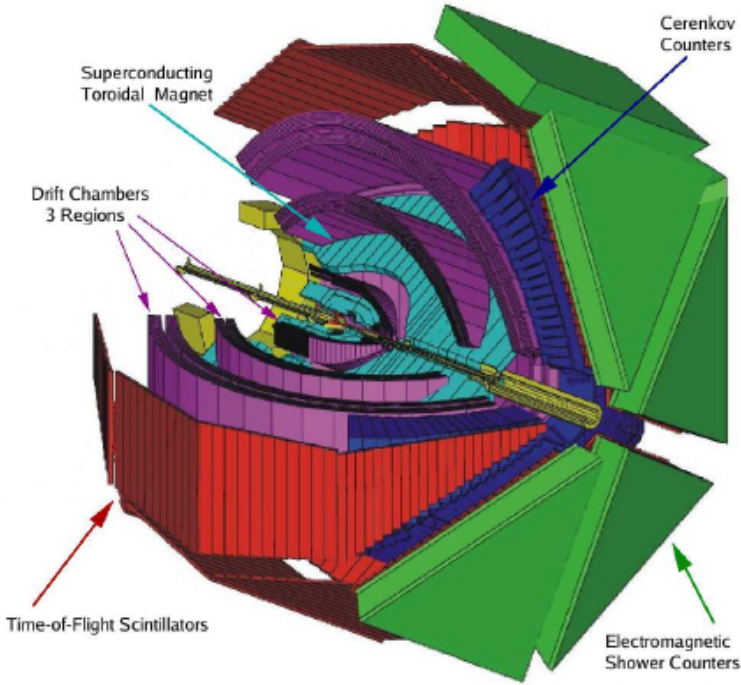


Figure 2.3: In this diagrammatic representation of CLAS, several important detector sub-systems are labeled.

halls. The beamline leading to the halls was also equipped with the ability to separate bunches before they completed five full passes delivering either three full energy beams, two full energy beams and one lower, or one full energy beam and two of lower energy. This capability, combined with the flexible beam polarization and beam current provided by the injector ensured that each hall could experiment at its desired settings simultaneously.

2.2 CLAS in Jefferson Lab Experimental Hall B

The CEBAF large acceptance spectrometer (CLAS), housed in Jefferson lab's Hall B, was used to record the E1-F dataset that is used in this study. Capable of detecting particles over a very large angular range, the CLAS detector covered almost the full 4π solid angle around the target region. The detector was also designed to perform efficiently for particles with wide range of momenta between 0.5-6.0 GeV. Overall detector design consisted of a large superconducting magnet that produced a toroidal field (this magnet was referred to as the torus), and six ideally identical *sectors*. Each sector of CLAS contained an identical set of sub-systems. After combining information from all sub-systems and running the reconstruction algorithm, complete events are measured. This capability made CLAS unique in comparison with the arm style spectrometers of halls A and C. The major components of CLAS are listed below.

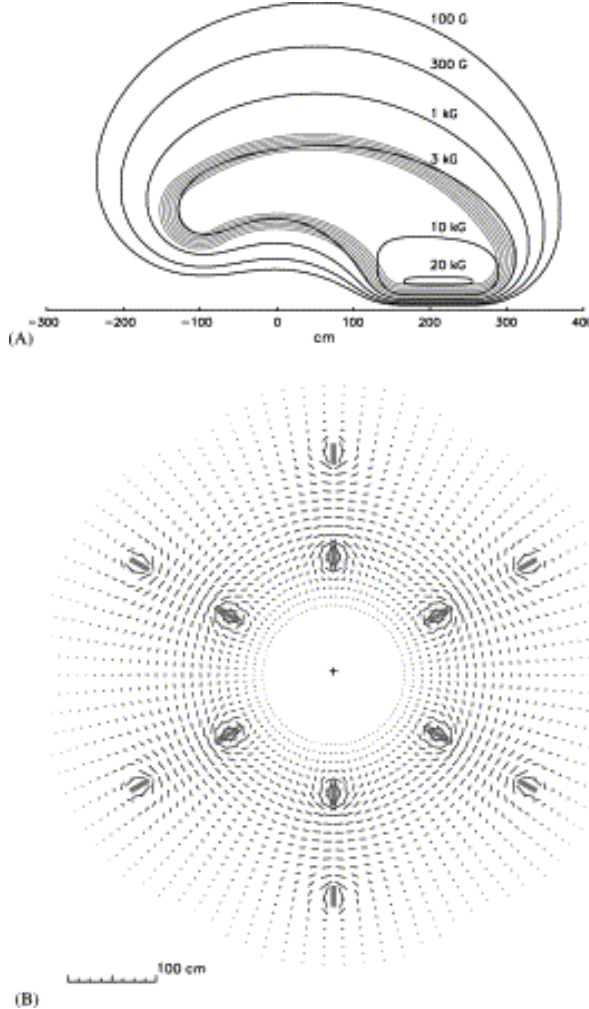


Figure 2.4: Diagrams of the CLAS torus field. This figure reproduced from [12]

2.2.1 CLAS Torus and Drift Chambers

Measuring the momentum of charged particles with $p > 200 \text{ MeV}/c$ was accomplished by measuring the curvature of the particle trajectory as it passed through the CLAS toroidal magnetic field. Six superconducting coils were arranged 60° apart azimuthally around the beamline to create a 2 Tesla. The field produced, which varied from two tesla at lower angles to half a tesla at angles greater than 90° , curved charged particle trajectories in the θ direction without altering the azimuthal ϕ direction. The geometry of the torus magnet guided the development of the entire spectrometer.

Spatially, the 18 drift chambers were divided with six in each sector. In order to perform tracking before, inside, and after the torus three radially distinct drift chambers were constructed for each sector (these were called regions 1, 2, and 3). Each drift chamber consisted of 12 superlayers of hexagonal drift chamber cells. Angular measurements in the azimuthal direction were accomplished by offsetting the first six and last six superlayers by 6° . In total 35,148 individual drift chambers cells were used for tracking [13].

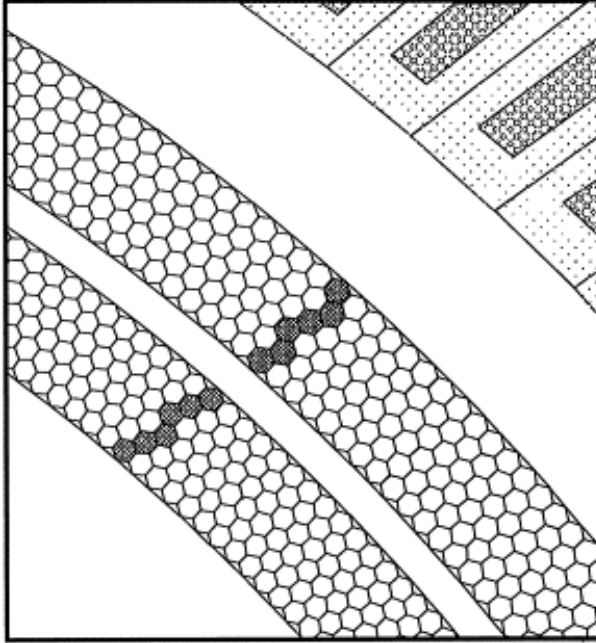


Figure 2.5: Illustration of a charged particle interacting with cells in the drift chamber. This figure was reproduced from [13]

2.2.2 CLAS Cherenkov Counter

The Cherenkov counters (CC), located radially outside of the region 3 drift chambers, greatly assisted in the separation of electrons and negatively charged pions for tracks with momentum less than the pion momentum threshold $p < p_\pi \approx 2.5 \text{ GeV}/c$ [12]. The CLAS CCs were divided into 6 sectors, like most other detectors. Each sector was divided into 18 segments in the polar angle θ away from the beamline. Furthermore, these segments were divided in half azimuthally to produce 12 half-sectors. Three mirrors, a light collecting Winston cone, a magnetic shield, and a 5 inch quartz face PMT were fitted to each of the 18 segments in all 12 half-sectors. During operation each CC was filled with 6 m^3 of C_4F_{10} gas. The number of photo-electrons produced was recorded for tracks with polar angles between $8^\circ < \theta < 45^\circ$.

2.2.3 CLAS Time of Flight Scintillator

Measurements of average velocity can be made by simply knowing the distance some object has traveled in a given time period. Operating on this principle the CLAS time of flight (TOF) system allowed for the separation of π and K for momentum $p \leq 2 \text{ GeV}/c$. Constructed of 57 scintillating bars per sector, the TOF system covered an impressive area of 206 m^2 and spanned the range of polar angles $8^\circ \leq \theta \leq 142^\circ$. Each of the scintillating bars measured 5.08 centimeters in thickness, 15 or 22 centimeters in width, and measured between 32 and 450 centimeters in length. Shorter bars, which covered the relatively higher rate low scattering angle, were built with an intrinsic timing resolution of 80 picoseconds.

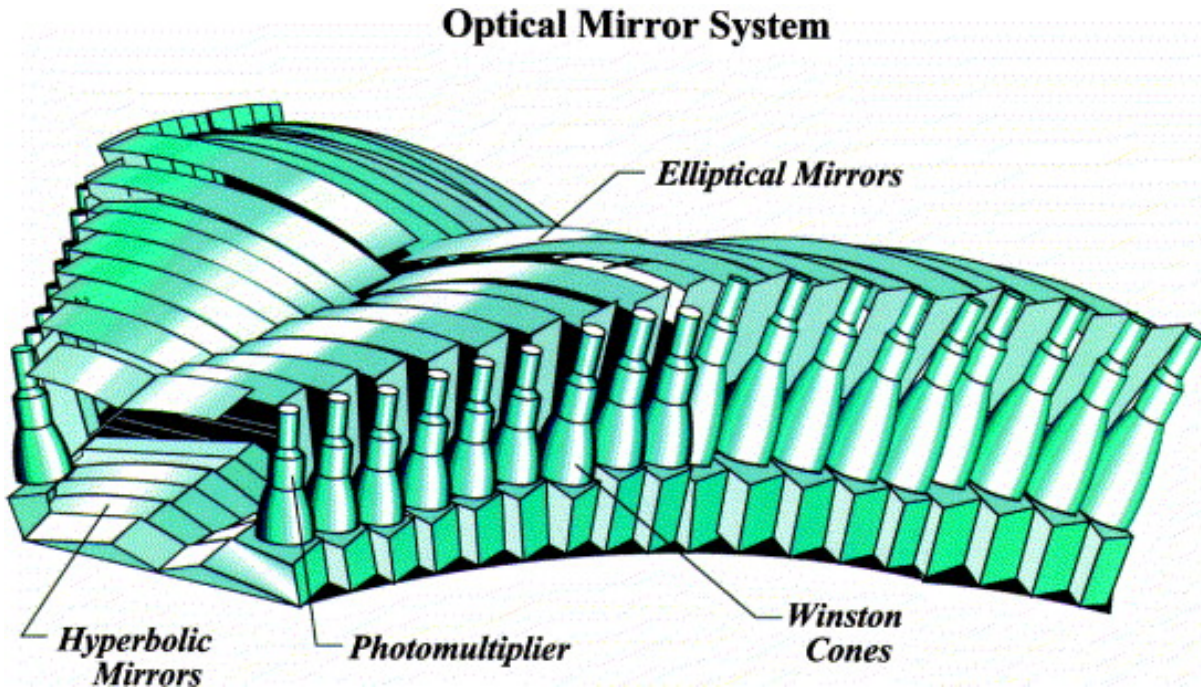


Figure 2.6: The CLAS Cherenkov Counter.

onds. The timing resolution for longer bars was designed to be 160 picoseconds, and measurements performed after the detector construction showed that the average timing resolution over the detector was 163 picoseconds [14].

During experiments where the electron beam was used, the start time for each event could be determined by assigning $\beta = 1$ to the fastest electron measured in the final state. However, once the tagger magnet was powered on and photon beam was delivered on target, start time information came from the start counter. Originally designed as six separate counters, the start counter was constructed with three counters spanning the full angular range of the detector. The target was surrounded by these three thin scintillators which had sufficient resolution to determine the difference between two sequentially arriving bunches ($\sigma \approx 350 \text{ ps}$).

2.2.4 CLAS Electromagnetic Calorimeter

The outermost layer of the CLAS detector was the electromagnetic calorimeter (EC). This sampling calorimeter was a main component of the CLAS trigger and had several important roles. Foremost, the EC detected and triggered on electrons with $E > 0.5 \text{ GeV}$. Detecting neutral particles such as photons and neutrons was a secondary role. By detecting photons with energies higher than 200 MeV, and having sufficient granular resolution, strongly decaying (π^0 or η) $\rightarrow \gamma\gamma$ particles were measured. Separation of neutrons and photons was achieved by combining information from the EC with timing information from the CLAS time of light system [15].

Structurally, the EC was composed in total of 1296 PMTs and 8424 scintillating strips in the six EC

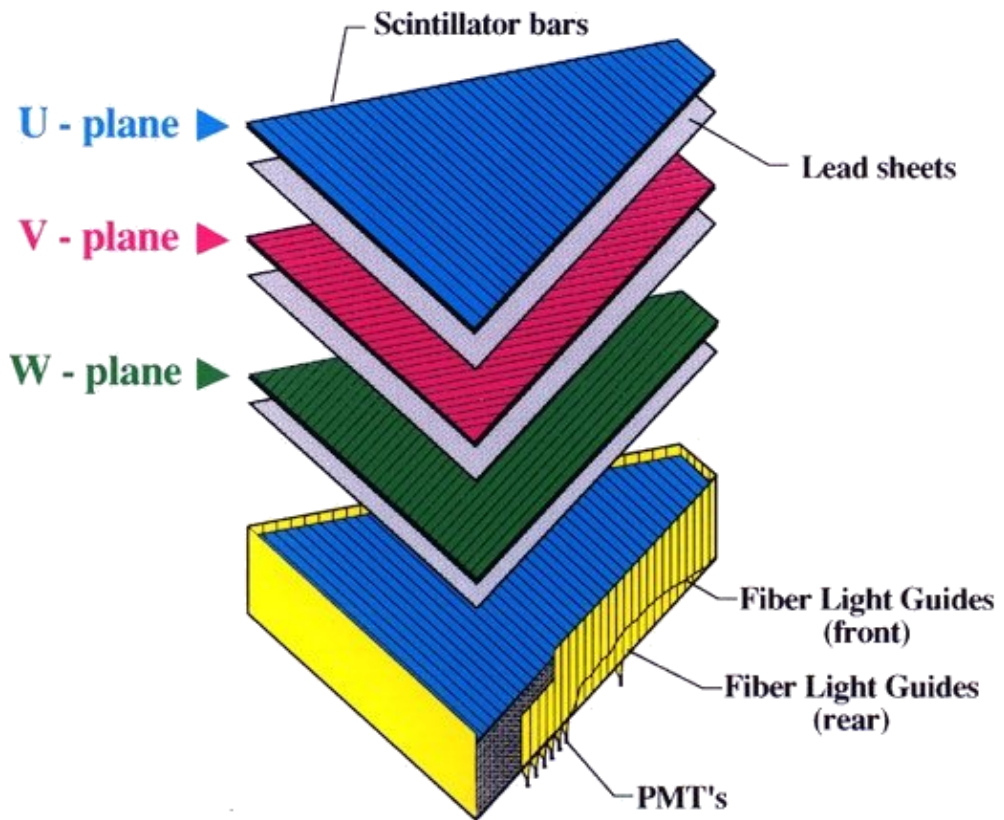


Figure 2.7: The U, V, W structure of CLAS electromagnetic calorimeter is shown above.

modules (one per sector). Alternating layers of lead and scintillator material were used to create a sampling fraction E_{dep}/p of approximately 0.3 for electrons. Measuring just 10 mm thick, and with a width of 10 cm (to balance cost of PMTs and granularity), the length of the scintillating strips depended on the angular location. Each EC module contained 3 sets of 13 layers offset by 120° to provide spatial information, these layers were referred to as U, V, and W.

2.2.5 E1-F

This study uses the dataset collected between April and July of 2003 known as E1-F. During this run period the beam energy was 5.498 GeV and the target was a 5cm liquid hydrogen cell. The torus current was set to 2250 Amperes, to maximize pion acceptance.

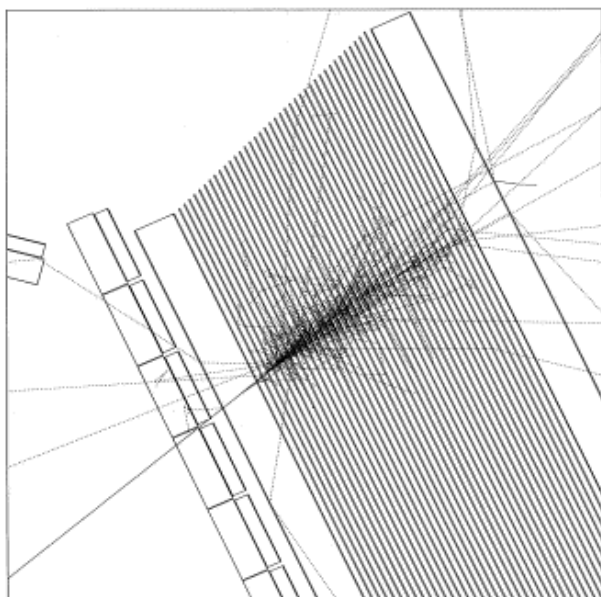


Figure 2.8: GEANT simulation of an electron showering in the EC. This figure originally appeared in [15]

Chapter 3

Basic Analysis & Corrections

3.1 Introduction

This chapter discusses analysis procedures that are common to the subsequent data analyses of kaons. These procedures can be divided into two groups. The first type of basic analysis described is the aggregation or calculation of scalar values over the run-period (examples include luminosity and helicity). The second type of analysis procedure described is a correction to measured values. Vertex corrections, timing corrections, and kinematic corrections will be discussed.

3.2 Determination of Good Run List

The total dataset contains 831 runs. Due to the complexities of the CLAS experimental setup, it is not uncommon for run conditions to change during a small percentage of the runs such that the data collected are not of analysis quality. For this reason, a good run list is constructed.

Good runs are selected for the list by counting good electrons in each file and normalizing by the accumulated charge for the associated file. While the number of events collected varies from run to run the ratio defined above is a stable quantity – provided that the run conditions do not vary greatly. Runs which are within 3 standard deviations of the mean (calculated over the dataset) are used as good runs. The good run list used for this analysis contains 522 runs.

3.3 Helicity Determination

During the course of the E1-F run period the beam helicity convention was changed by the insertion of a half-wave plate at the injector. The definition of \pm helicity must change in accordance with these

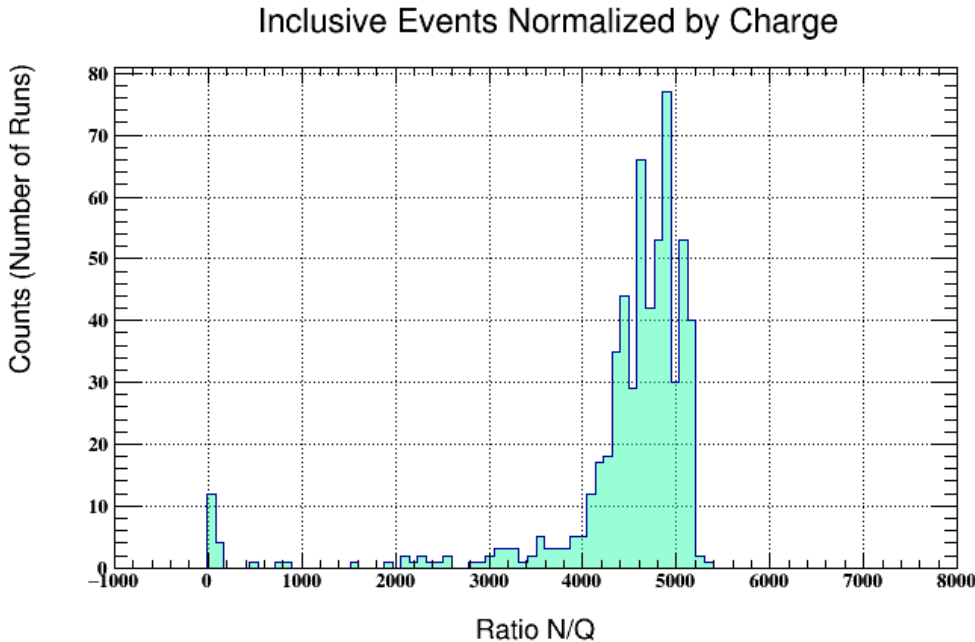


Figure 3.1: Inclusive electrons per file normalized by the total charge accumulated for the file. This quantity is used to make a good run list.

wave-plate insertions. To monitor these changes, the value of $A_{LU}^{\sin \phi}$ for π^+ is recorded for every run. Whenever the asymmetry (which has a magnitude of around 3%) changes sign, the sign convention has changed. These changes are taken into account in the data analysis.

3.4 Vertex Corrections

The track vertex position (v_x, v_y, v_z) is calculated based on the intersection of each track with the mid-plane (the plane which contains the beamline and bisects the sector at $\phi_{rel} = 0$). If the beam is not centered at $(x, y) = (0, 0)$, the vertex position calculation needs to be corrected by shifting the mid-planes in accordance with the target offset. The offset (x, y) is identified by plotting events from the control foil placed near the target, which has a z position of -20 cm. For the E1-F run period, the beam position was $(0.15, -0.25)$ cm.

3.5 Timing Corrections

Timing information comes from the time-of-flight detector system. After calibration, small offsets in timing between time of flights paddles still exist for the E1-F dataset. These biases can be removed on a run-by-run and paddle-by-paddle basis by adding a small shift t_{corr} . In order to determine this shift

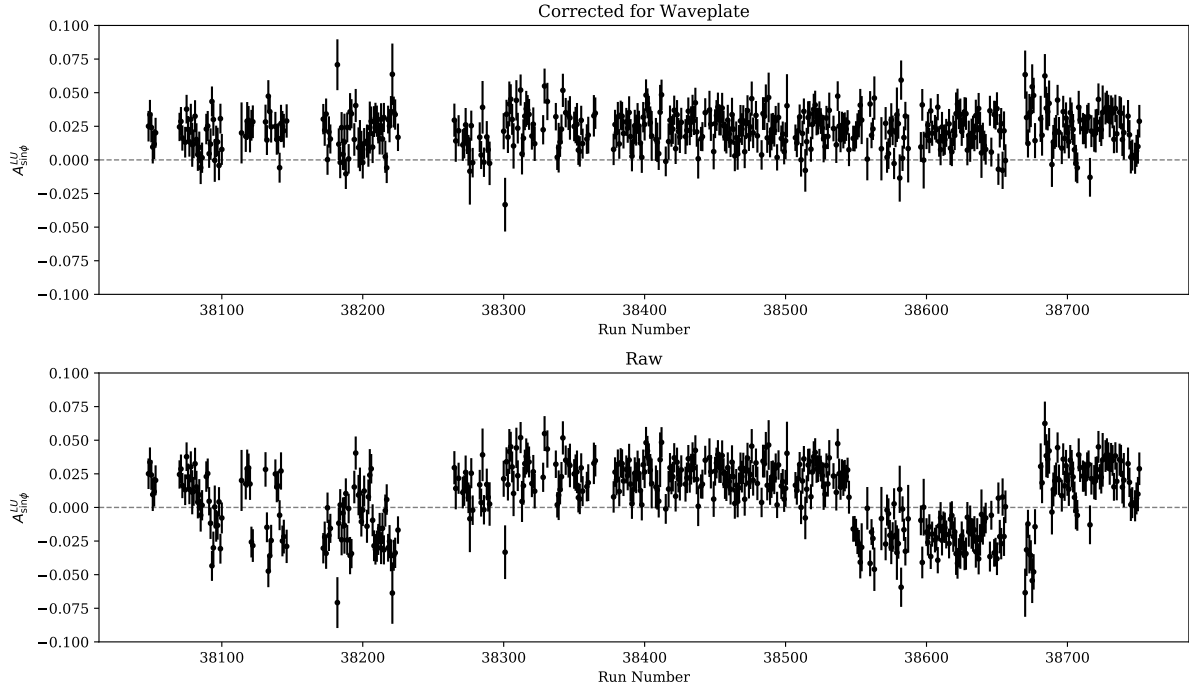


Figure 3.2: The waveplate position is determined and corrected by plotting the BSA for π^+ mesons as a function of the run. The top panel shows the corrected results, the bottom shows the results before changing the helicity.

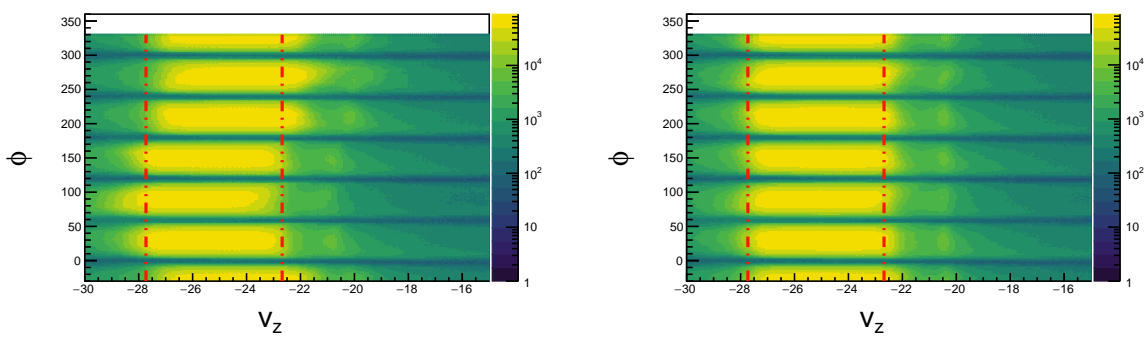


Figure 3.3: The z-vertex v_z position shown for different values of ϕ the azimuthal angle in the hall. The left figure shows the distribution before corrections are applied, the right after. The vertical red lines bound the region which we define as acceptable for electrons in our analysis.

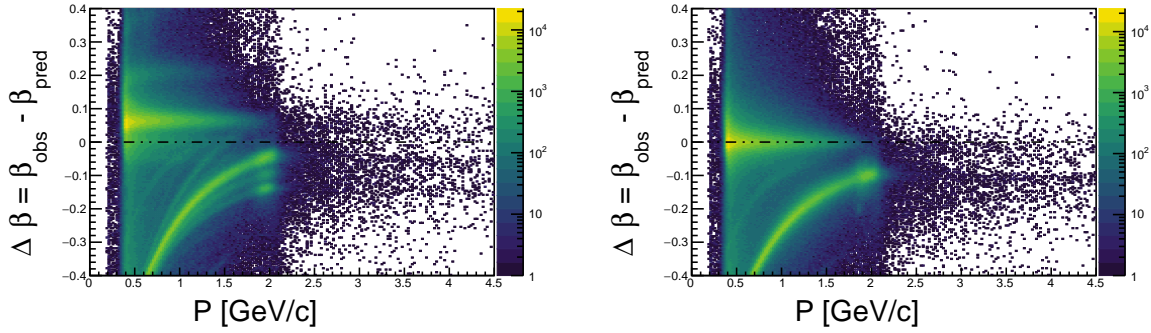


Figure 3.4: Timing corrections are shown for paddle 24 of sector 1. The left image shows the $\Delta\beta$ distribution before corrections. On the right the same is shown after correction of the timing for this paddle. We assume the mass of the track to be the pion, these show up as the green band. Heavier protons are visible below the pion band.

t_{corr} for each paddle, charged pions are used.

Using momentum information from the drift chambers the value of β can be predicted and the difference $\Delta\beta$ can be determined for each pion.

$$\Delta\beta = \beta_{obs} - \beta_{pred} = \frac{d}{ct_{obs}} - \sqrt{1 + (m/p)^2} \quad (3.1)$$

Here m is assumed to be m_π . The offset $\Delta\beta$ from 0 is used to define the value of t_{corr} for each paddle. If this value is exceedingly small, no correction is applied. For some paddles with low statistics a reasonable value for t_{corr} cannot be obtained and these paddles are excluded from the analysis.

In the method described above, the calibrated paddle is the one which is struck by the pion. The electron paddle which was struck could also require calibration. In practice the magnitude of the correction term t_{corr} is small, and the paddle offset is (likely) randomly distributed about 0 when considering all paddles. By including events from many different (electron) paddles, miscalibration effects from the electron side cease to be important. This is demonstrated by the success of the technique in centering the $\Delta\beta$ distributions. This work was first described in [16].

3.6 Kinematic Corrections

The magnetic field map used in reconstruction to swim particle tracks cannot perfectly match the real magnetic field of the hall. As a result of this the reconstructed momentum of particles is often slightly off (of order 1%). Small misalignments in detector positions also contribute to this effect. In order to

correct for these small differences, the momentum (p_x, p_y, p_z) and hence θ of charged tracks is corrected.

Various procedures exist for the correction of kinematic variables of measured particles, and they all rely on energy and momentum conservation applied to standard processes (such as elastic scattering). The procedure used to derive corrections for the E1-F dataset was developed and described by Marco Mirazita in [17].

As mentioned previously, the need for correction to θ (the polar angle measured from the beamline) arises from misalignments in the drift chambers. This implies that the correction will be the same for positives and negatives, and this assumption is used in the correction algorithm. First, elastic ($ep \rightarrow ep$) events are selected by identifying events that contain at least one electron and one proton, then requiring that the missing mass M_X of the ($ep \rightarrow epX$) system is close to 0. The kinematics of the event are then calculated.

$$k^\mu = (k, 0, 0, k) \quad (3.2)$$

$$p^\mu = (M_p, 0, 0, 0) \quad (3.3)$$

$$k'^\mu = (k', k' \sin \theta, 0, k' \cos \theta) \quad (3.4)$$

$$p'^\mu = (E_p, -p' \sin \alpha, 0, p' \cos \alpha) \quad (3.5)$$

Applying energy and momentum conservation to the equations above yields 3 equations.

$$k + M_p = k' + \sqrt{M_p^2 + p'^2} \quad (3.6)$$

$$k' \sin \theta = p' \sin \alpha \quad (3.7)$$

$$k = k' \cos \theta + p' \cos \alpha \quad (3.8)$$

Using these equations, the electron angle θ and the proton angle α can be predicted by using the momenta (k', p'). These values are compared with measured values and iteratively corrected by tuning the parameters of a phi-dependent 2nd order polynomial.

$$\cos \theta = 1 - M_p \frac{k - k'}{kk'} \quad (3.9)$$

$$\tan \alpha = \frac{1}{p'} \frac{k' \sin \theta}{k - k' \cos \theta} \quad (3.10)$$

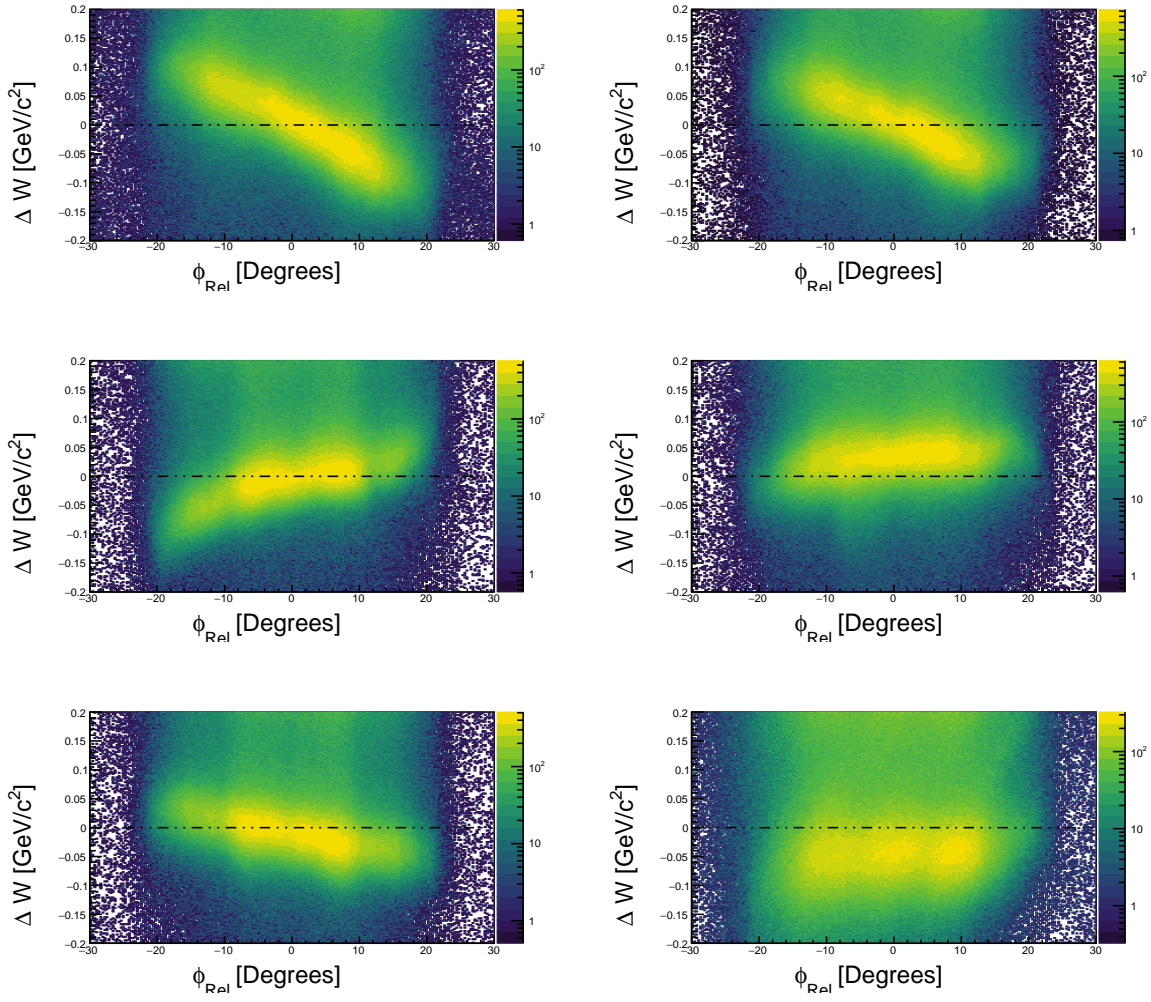


Figure 3.5: This figure shows the deviation from M_p of the W spectrum peak for elastic $ep \rightarrow ep$ events (before corrections).

After θ corrections are applied, the momentum of the electrons are corrected by using an analogous procedure for k' instead of θ and α . The momentum corrections are calculated as functions of ϕ for each sector in one degree bins of θ . Finally, the positively charged particles momenta are corrected by selecting the exclusive event ($ep \rightarrow e\pi^+ N$). In this reaction the scattered electron and pion are detected and the neutron is selected using a missing mass cut. Assuming the electron momentum, electron angle, and pion angle to be correct, the pion momentum correction is then calculated by iteratively improving the central position of the neutron mass peak to coincide with M_N . Marco Mirazita shows in his note that these corrections can be satisfactorily applied to all negative and positive particles.

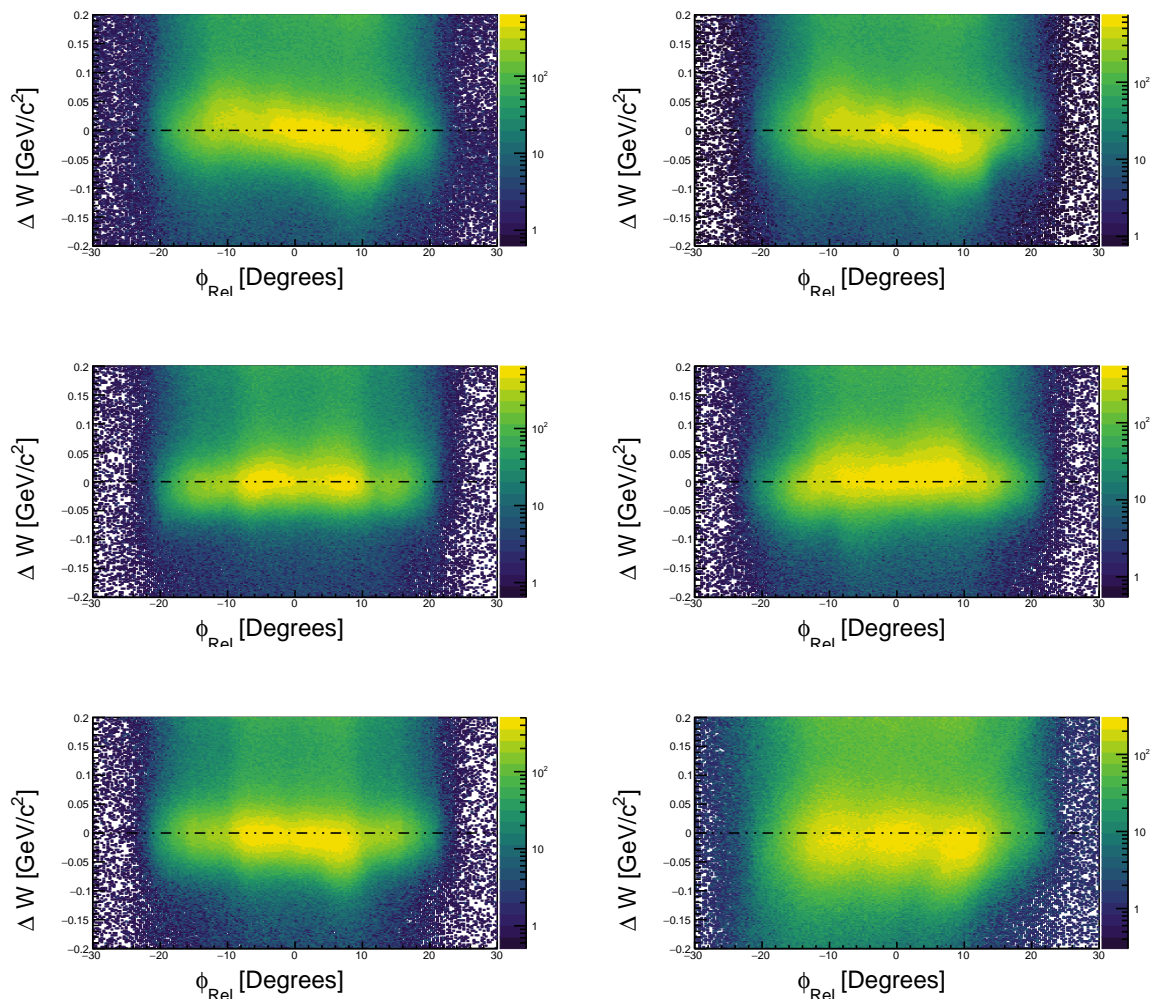


Figure 3.6: This figure shows the deviation from M_p of the W spectrum peak for elastic $ep \rightarrow ep$ events (after ϕ -dependent corrections).

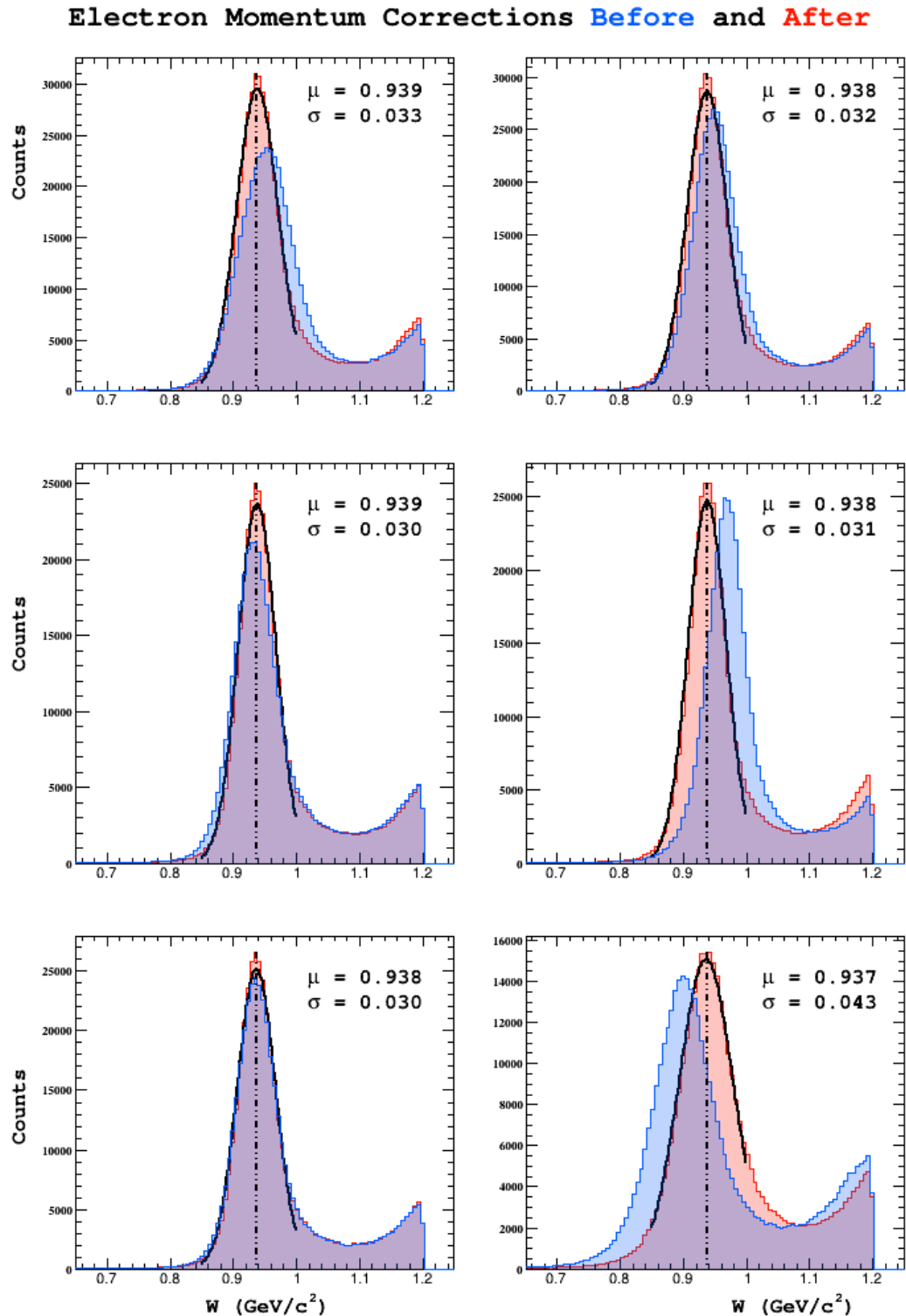


Figure 3.7: Elastic events shown in the spectrum of W before and after momentum corrections are applied.

Chapter 4

Particle Identification

4.1 Introduction

Particle identification (PID) is the process of classifying tracks as known particles. After reconstruction and matching of detector responses to each track, the reconstruction package `reccsis` assigns a preliminary particle identification based on loose selection criteria. In this analysis, tracks are classified based on a more stringent criteria. This chapter discusses the methodology used to classify particles.

4.2 Electron Identification

Electrons in CLAS are abundant, and the detection of an electron is a basic necessity for every event that will be analyzed. The most naive approach to performing electron identification would be to call all negatively charged tracks electrons. Doing this would provide an extremely efficient identification of electrons (none of them are missed), however the purity of the sample (the fraction of tracks identified as electrons that are actually electrons) would be low due to the vast quantity of negatively charged pions that are produced in during the experiment. Additionally, doing this would completely eliminate the possibility of identifying negatively charged pions or kaons, as all negative tracks would be called electrons. In practice then, the identification of electrons is concerned with removal of negative pions and kaons from the sample of negative tracks. This is accomplished by applying a series of cuts on measured variables that distinguish between electrons and pions (pions are the dominant background).

4.2.1 Electron ID Cuts

The cuts used to select electrons are enumerated below.

- Negative charge

- Drift chamber region 1 fiducial
- Drift chamber region 3 fiducial
- Electromagnetic Calorimeter fiducial (UVW)
- EC minimum energy deposition
- Sampling Fraction (momentum dependent)
- z-vertex position
- Cherenkov counter θ_{cc} matching to PMT number
- Cherenkov counter ϕ_{rel} matching to PMT (left/right)

Each cut is now described in more detail.

Negativity Cut

Each track is assigned a charge based on the curvature of its trajectory through the magnetic field of the torus. This is done during the track reconstruction phase. Tracks are eliminated as electron candidates if they are not negatively charged.

Drift chamber fiducial

The fiducial region or volume is a term used to refer to the region of a sensitive detector which is unimpeded in its acceptance of physics events. In practice, shadows from other detectors, poorly understood edge effects, or geometric obstacles may impede the flight of particles from the target, and render regions of sensitive detectors unreliable (to use the vocabulary presented above, these events fall outside of the fiducial region of the detector).

Negative tracks which pass geometrically close to the edges of the drift chamber are, from a tracking perspective, more difficult to understand. Additionally, tracks which fall outside of the fiducial region of the drift chambers are likely to fall outside of the fiducial region of the downstream detectors as well. For these reasons, it is common to remove tracks which are geometrically close to the boundaries of the drift chambers in region 1 as well as region 3 coordinate systems.

To implement this cut the (x, y) coordinates of the drift chambers are rotated into one sector. Then boundaries y_{left}, y_{right} are defined as linear functions of x . The boundary lines are parametrized by an offset h and an angle of the boundary line with respect to the center of the sector at $x = 0$. The slope of these lines is $\pm \cot(\theta)$.

Region	Height h (cm)	Angle θ (degrees)
1	22	60
3	80	49

Table 4.1: Cut parameters used for the DC fiducial cut.

EC Coordinate	Min (cm)	Max (cm)
U	70	400
V	-	362
W	-	395

Table 4.2: Cut parameters used for the EC fiducial cut.

$$y_{right} = h + \cot(\theta)x \quad (4.1)$$

$$y_{left} = h - \cot(\theta)x \quad (4.2)$$

Tracks passing this criterion are those which have $y > y_{left}(x)$ and $y > y_{right}(x)$.

Electromagnetic Calorimeter fiducial (UVW)

As particles traverse the electromagnetic calorimeter they develop electromagnetic showers. If the track passes close to the edges of the detector, there is a chance that the shower will not be fully contained within the calorimeter volume (it spills out the edges). For this reason, it is standard to remove the hits which fall within the outer 10 centimeters of each layer of the EC (10 centimeters is the width of a scintillator bar). This cut is applied in the U, V, W coordinate system.

EC minimum energy deposition

One way to differentiate between these electrons and pions is to exploit the difference in energy deposition between the two in the electromagnetic calorimeter. Electron typically develop a much larger and more energetic shower than π mesons, which minimally ionize the calorimeter material. The result is that the total energy deposition is typically larger for electrons than π mesons. In this analysis we require that at least 60 MeV was deposited in the inner calorimeter for electron candidates.

Sampling Fraction (momentum dependent)

The electromagnetic calorimeter is designed such that electrons will deposit $E_{dep}/p \approx 0.3$ approximately one-third of their energy, regardless of their momentum. In contrast to this, the ratio E_{dep}/p for π mesons decreases rapidly with momentum. To develop a momentum dependent cut for this distribution, all negative candidates are first filled into a two-dimensional histogram of E_{dep}/p vs. p . The histogram is then binned more coarsely in momentum, and projected into a series of 40 momentum

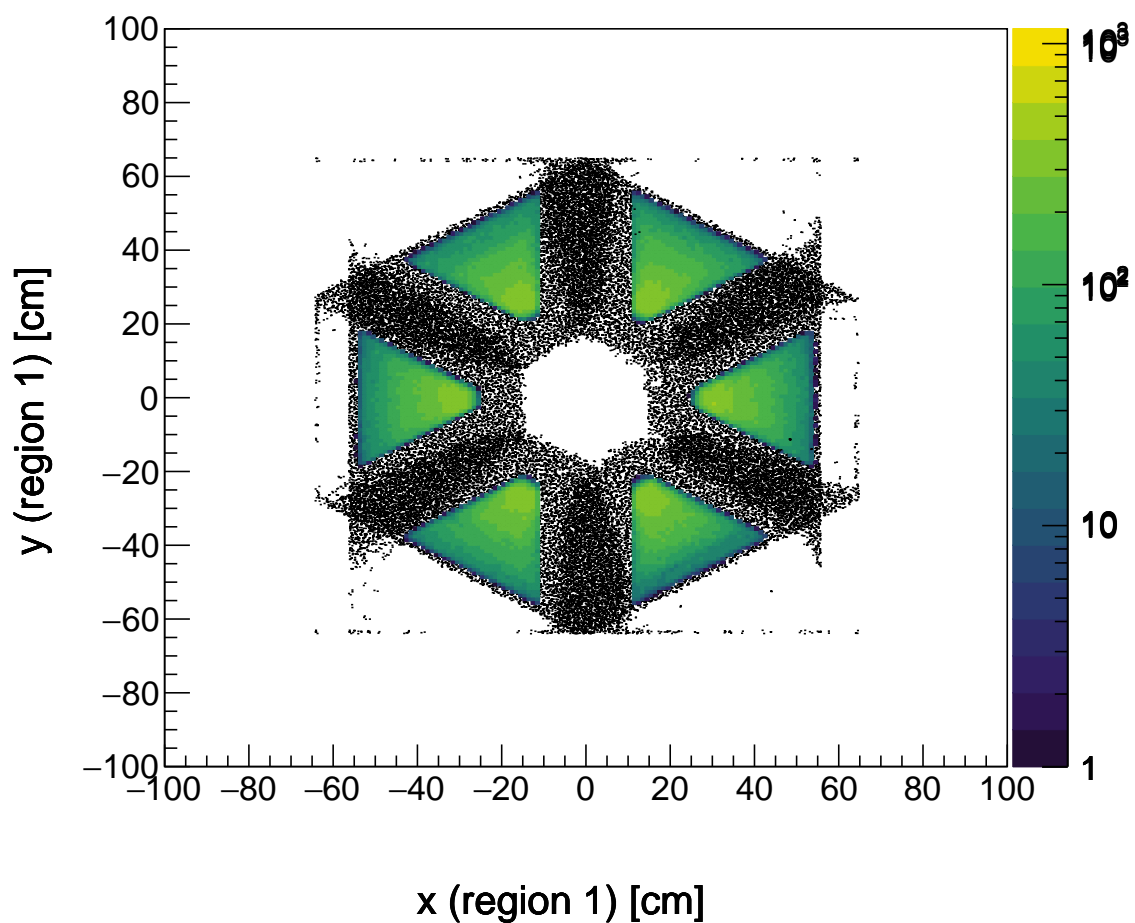


Figure 4.1: Tracks shown in color remain after the application of drift chamber region 1 fiducial cuts to all cuts, shown here as black points.

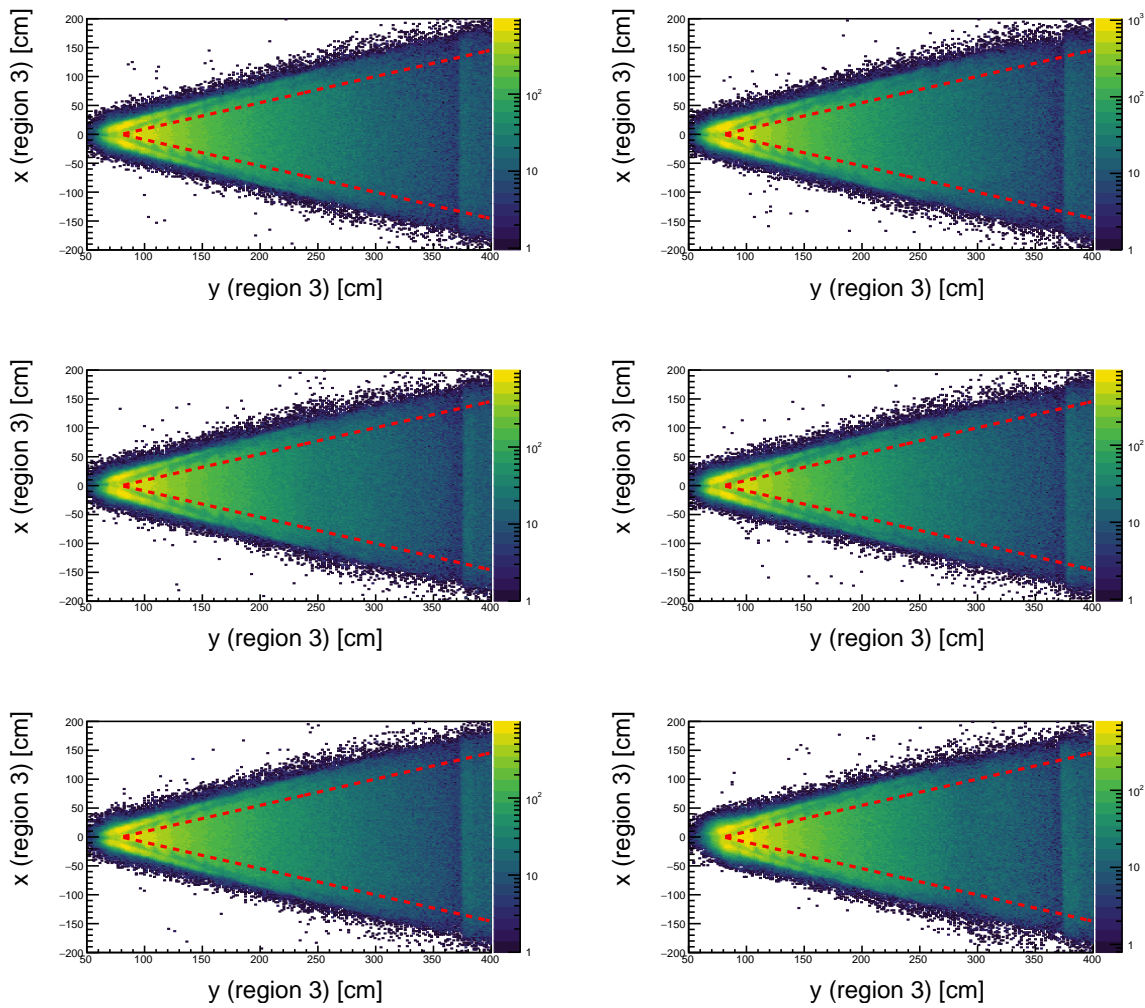


Figure 4.2: The selection criteria shown in red is applied to drift chamber region 3.

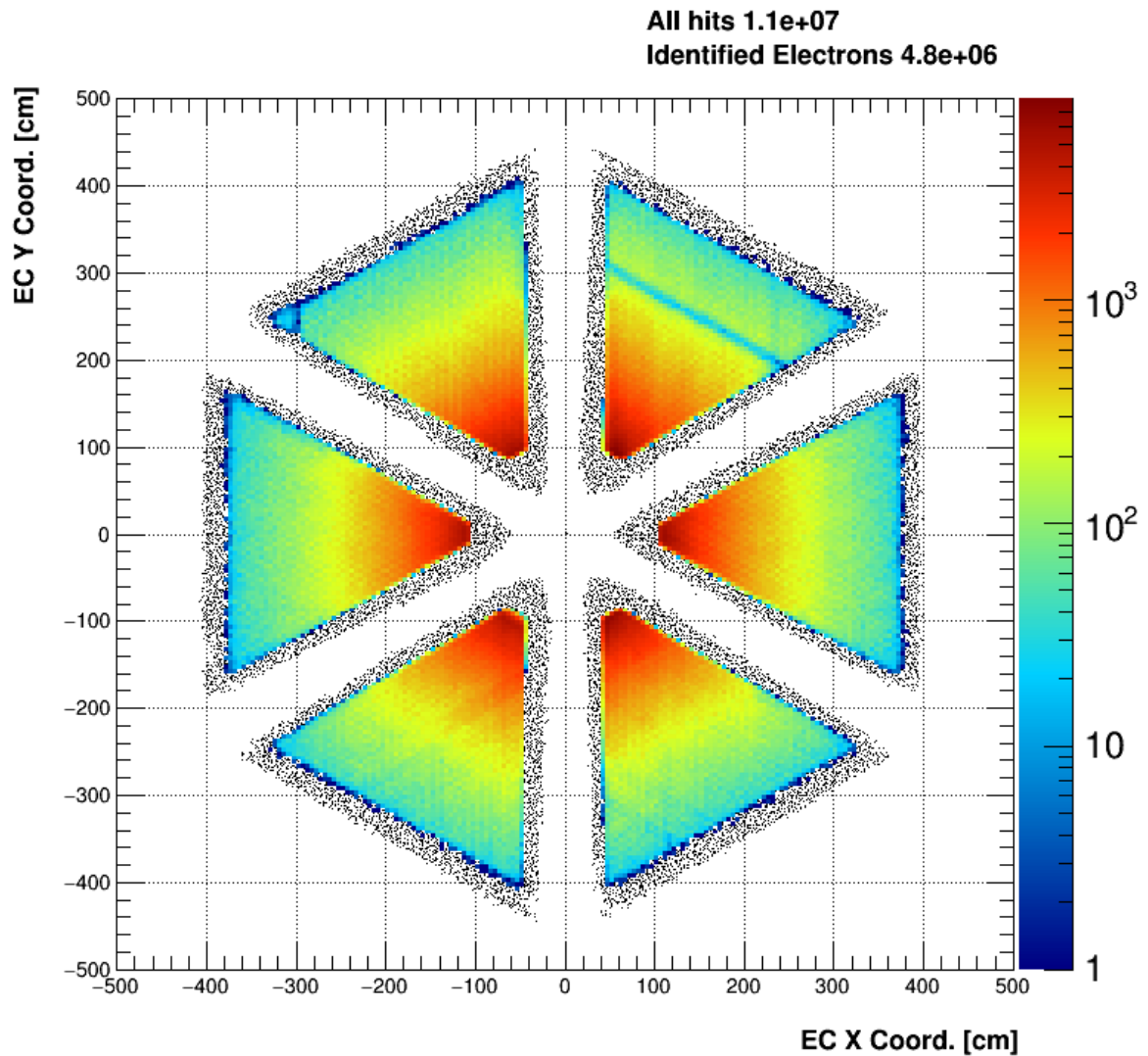


Figure 4.3: All negative tracks are shown here in black. In color, the tracks which pass the EC fiducial cut are shown.

slices. Each of these slices is fit with a Gaussian to extract the position μ_i and width σ_i of the electron peak. Finally, a functional form for the mean and standard deviation of the distributions is chosen to be a third order polynomial in momentum.

$$\mu(p) = \mu_0 + \mu_1 p + \mu_2 p^2 + \mu_3 p^3 \quad (4.3)$$

$$\sigma(p) = \sigma_0 + \sigma_1 p + \sigma_2 p^2 + \sigma_3 p^3 \quad (4.4)$$

Boundaries are constructed from this information by adding (subtracting) n_σ from the mean. In the nominal case, we use $n_\sigma = 2.5$.

$$f_{max}(p) = \mu(p) + n_\sigma \sigma(p) = (\mu_0 + n_\sigma \sigma_0) + (\mu_1 + n_\sigma \sigma_1)p + (\mu_2 + n_\sigma \sigma_2)p^2 + (\mu_3 + n_\sigma \sigma_3)p^3 \quad (4.5)$$

$$f_{min}(p) = \mu(p) - n_\sigma \sigma(p) = (\mu_0 - n_\sigma \sigma_0) + (\mu_1 - n_\sigma \sigma_1)p + (\mu_2 - n_\sigma \sigma_2)p^2 + (\mu_3 - n_\sigma \sigma_3)p^3 \quad (4.6)$$

Due to slight differences between the 6 sectors of the CLAS detector, this cut is calibrated and applied for each sector individually. Results are shown in table 4.3.

Parameter	Sector 1	Sector 2	Sector 3	Sector 4	Sector 5	Sector 6
μ_3	-8.68739e-05	0.000459313	9.94077e-05	-0.000244192	-7.65218e-05	-0.000392285
μ_2	-0.000338957	-0.00621419	-0.00267522	-0.00103803	-0.00222768	-0.00105459
μ_1	0.0191726	0.0393975	0.02881	0.0250629	0.0233171	0.0265662
μ_0	0.2731	0.296993	0.285039	0.276795	0.266246	0.25919
σ_3	-0.000737136	0.000189105	-0.000472738	-0.000553545	-0.000646591	-0.000633567
σ_2	0.00676769	-0.000244009	0.00493599	0.00434321	0.00717978	0.00626044
σ_1	-0.0219814	-0.00681518	-0.0180929	-0.0140827	-0.0246181	-0.022029
σ_0	0.0474188	0.0475098	0.0461743	0.0492728	0.0546257	0.0517508

Table 4.3: μ and σ values used to construct the momentum dependent sampling fraction cut.

z-vertex position

Electrons can be produced as part of e^+e^- pairs, or by other processes. For this analysis, these are not of interest. For the purposes of this analysis it is then natural to accept only electron candidates which have a z-vertex $v_z \in [-27.7302, -22.6864]$ within the expected target region. This cut is applied after the vertex position has been corrected (which is discussed in the basic analysis section).

Cherenkov counter θ_{cc} and ϕ_{rel} matching to PMT

The angular arrangement of photo-multiplier tubes (PMTs) in the Cherenkov counter allows for additional consistency conditions to be applied. Each half-sector of the CC contains 18 PMTs increasing in polar angle away from the beamline, these divisions are known as segments. The polar angle measured

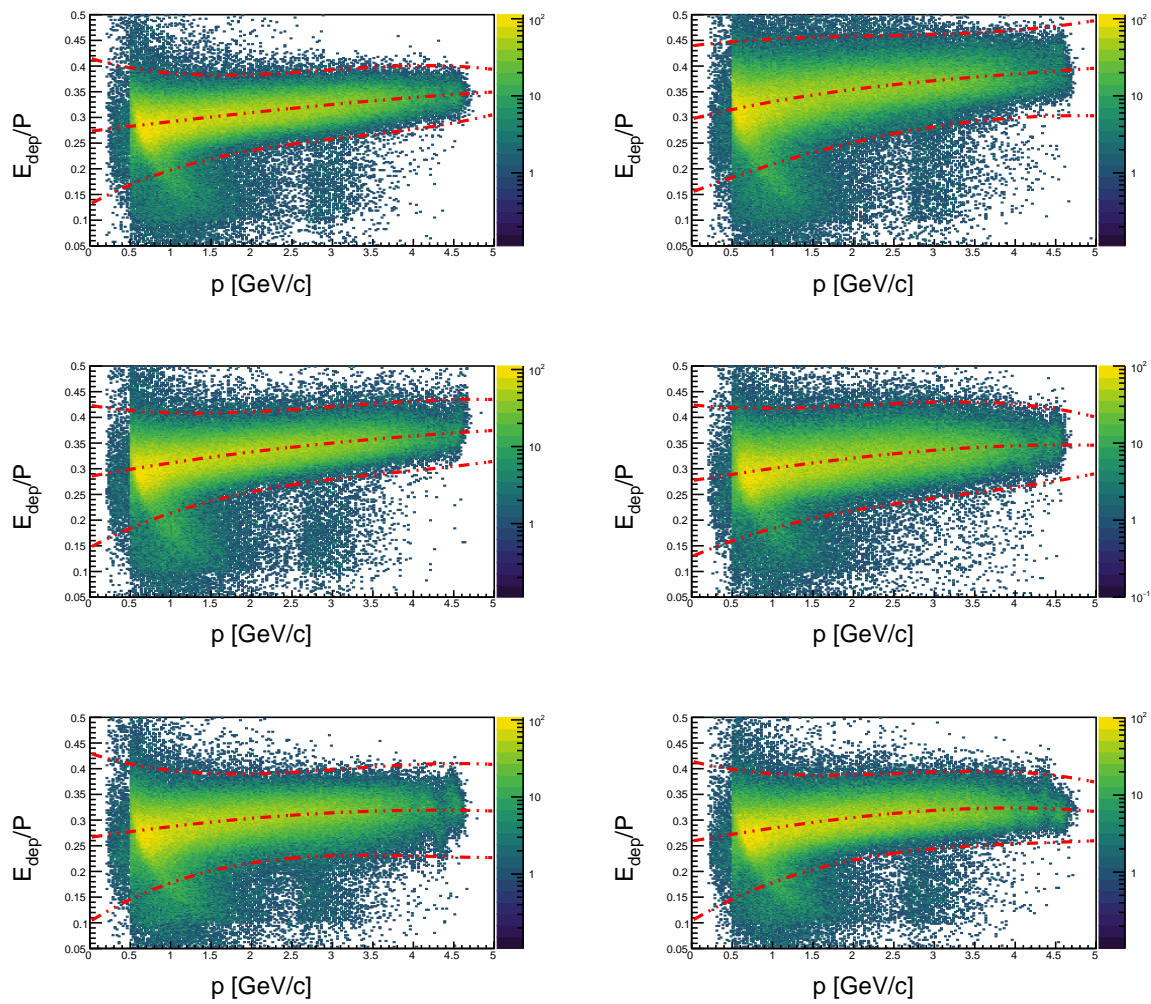


Figure 4.4: The sampling fraction selection boundary is shown here for the nominal value of $N_{sigma} = 4$.

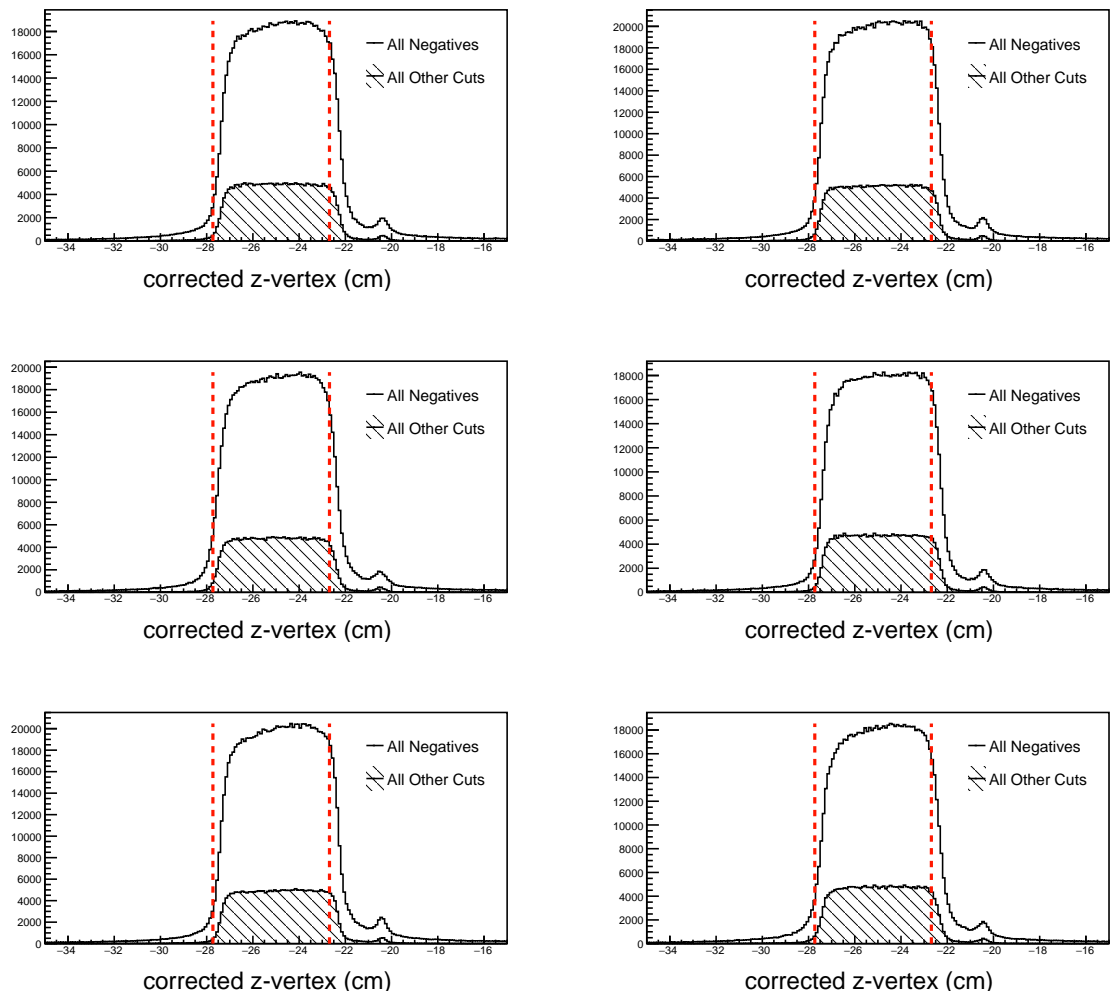


Figure 4.5: The track vertex cut is shown above. All negative tracks are shown in white, while the tracks passing all other criteria are shown in black hatch. The cut boundary is displayed as red lines. For E1-F the target center was located at -25 cm.

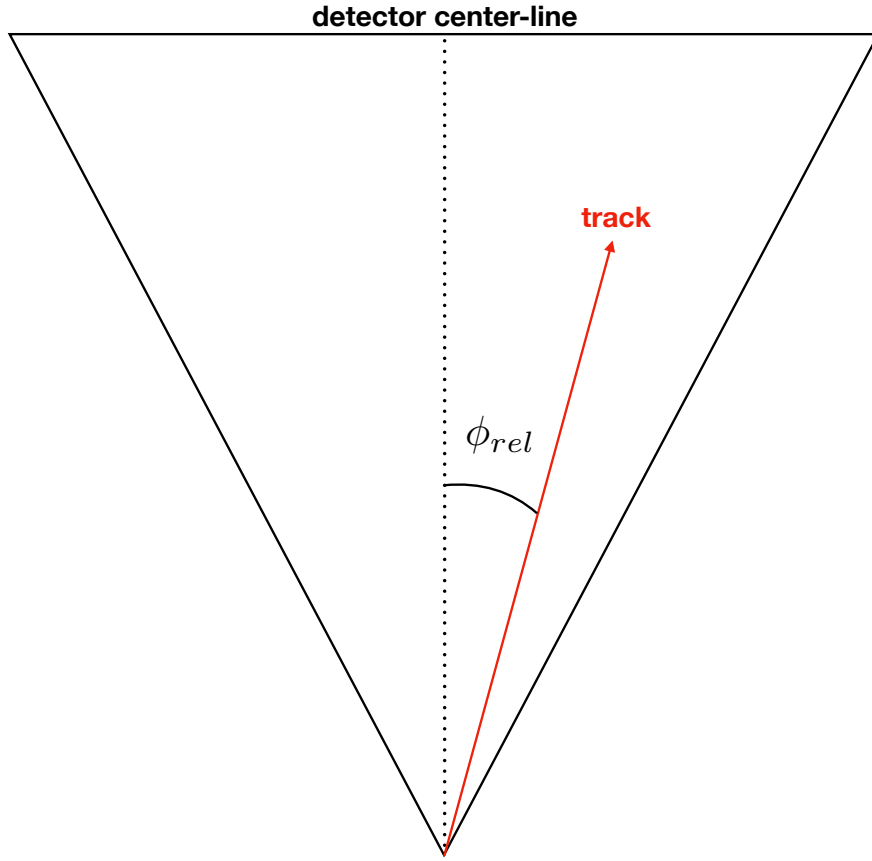


Figure 4.6: The angle ϕ_{rel} is the azimuthal angle between the central line of the detector and the track.

at the Cherenkov counter θ_{cc} is then correlated to the segment in which the track was detected. Additionally, PMTs that are placed on the left and right of the detector can be used to check consistency with the azimuthal angle the track forms with the central line of the detector (ie $\phi_{rel} > 0$ means the track was in the right half of the sector, $\phi_{rel} < 0$ means the track was in the left half of the sector). An integer is used to describe the PMT associated with the track. The left PMT is assigned value -1, the right 1, and a signal in both PMTs is assigned 0. If both PMTs have a signal, the track is allowed to pass. If the left PMT was the one that had a signal, only events with $\phi_{rel} < 0$ passes. Similarly if the right PMT fired (code = 1), only events with $\phi_{rel} > 0$ are allowed to pass. Technical note: the integers in question can be obtained from the ntuple22 format tree by doing the following.

```

for (int index = 0; index < event.gpart; index++) {
    int pmt = event.cc_segm[index]/1000 - 1;
    int segment = event.cc_segm[index]%1000/10;
}

```

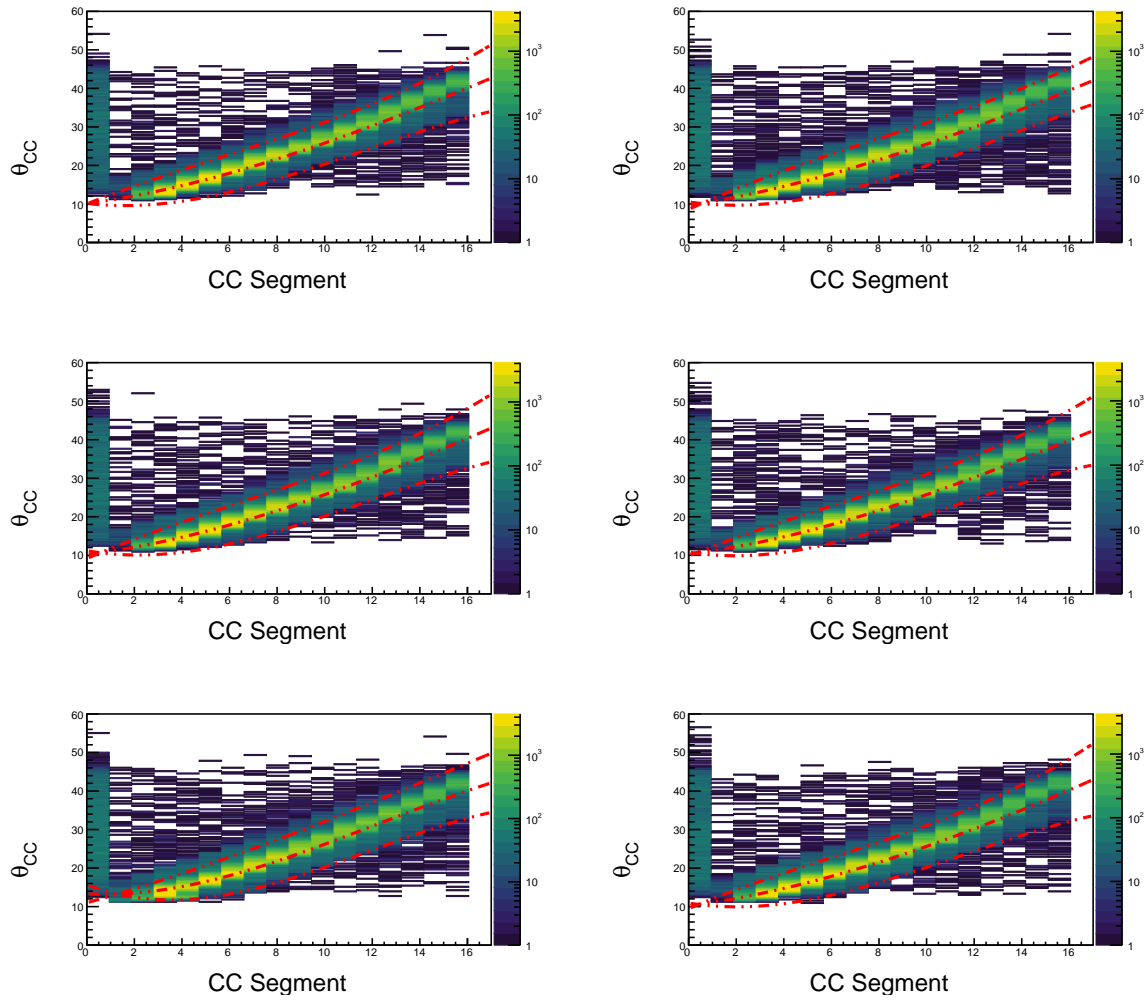


Figure 4.7: Correlation between θ_{CC} and the CC segment is shown above, with our selection boundaries overlaid in red.

4.3 Hadron Identification

Hadron identification in CLAS is done by correlating particle momentum from the drift chambers with timing information supplied by the time of flight detector. In this analysis some quality assurance cuts are applied preliminarily, but they do not discriminate between different species of particle. The likelihood methodology described in this section is based on the discussion provided by the BES collaboration in [18].

4.3.1 Hadron ID Cuts

The cuts used for hadron classification are enumerated below.

- Drift chamber fiducial
- Hadron-electron vertex difference
- Likelihood maximization of $\beta(p, h)$

Drift chamber fiducial

Drift chamber fiducial cuts are applied (only region 1) using the same procedure as described for electrons. The parameters are for negative hadrons are those which are used for the electron. The parameters used for positive tracks are $h = 10, \theta = 60$.

Hadron-electron vertex difference

The distance between the electron vertex and the hadron candidate track vertex is computed ($\delta v_z = v_z^e - v_z^+$). This distance is constrained to be within the length of the target (5 cm) see figure 4.3.1. This cut would not be applicable to studies where a significantly detached vertex is expected.

Likelihood maximization of $\beta(p, h)$

In this section, positive hadrons are used as an example. The same method is applied to the negative hadrons. For each particle species considered, a normalized probability density function $P(x; p, h)$ is constructed for each input into the likelihood analysis. Here, x corresponds to the feature being used to categorize different particles (in our case, x is the β value measured by CLAS time-of-flight), p is the particle momentum, and h is the hadron being hypothesized (eg: the possible values for positive hadrons are pion, kaon, proton). In general if one uses a set of N variables $x = (x_1, x_2, \dots, x_N)$, the likelihood for a hypothesis h is defined below.

$$\mathcal{L}_h = \prod_{i=1}^N P_i(x_i; p, h) \quad (4.7)$$

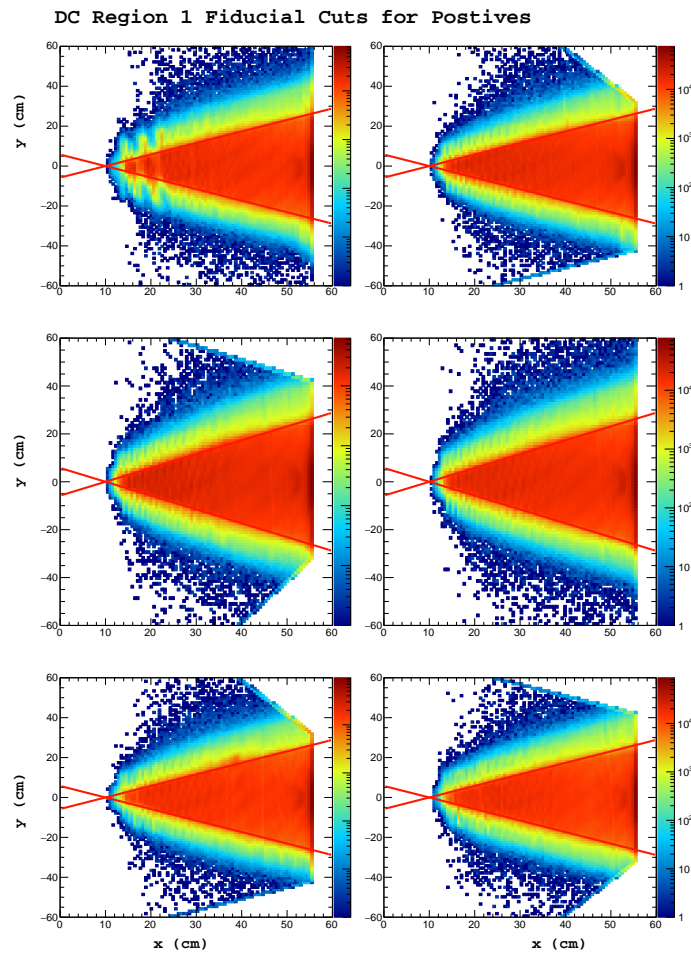


Figure 4.8: Shown above: Positive track hits on the region 1 drift chamber, events falling between the red lines are kept for analysis.

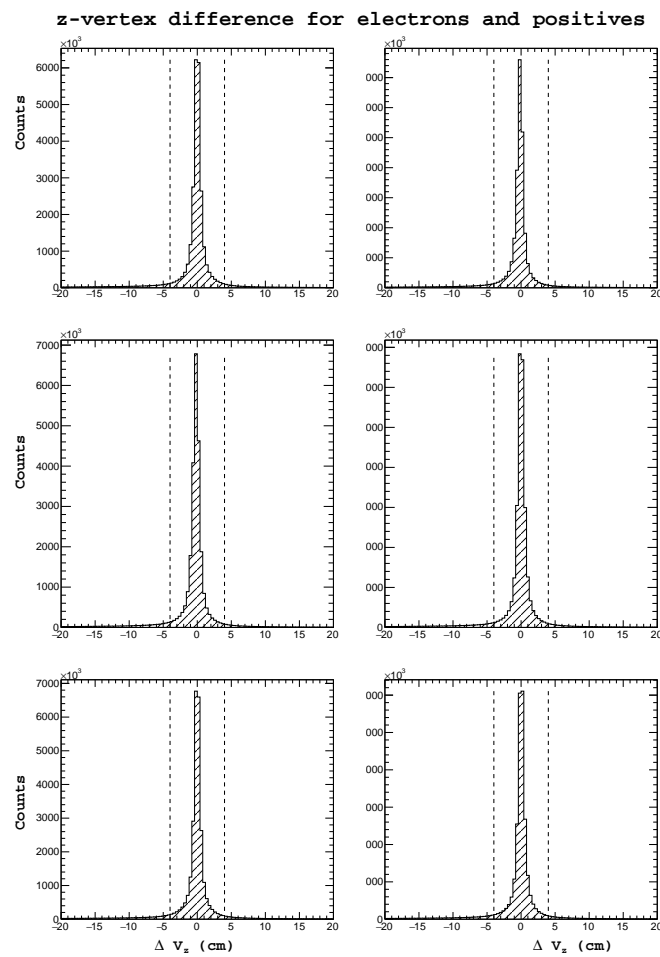


Figure 4.9: Shown above: The difference between the z-vertex position between detected electrons and positive tracks.

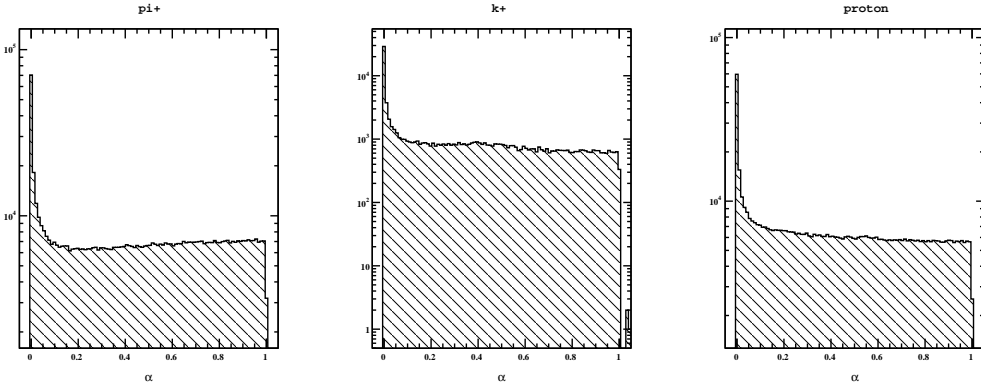


Figure 4.10: Shown above: The distribution of confidence level for all positive tracks after being classified by the likelihood ratio.

In our case, the only random variable we consider is β , and the likelihood is just the PDF. Here, and in many cases where the choice is statistically appropriate, it is possible to use a Gaussian PDF for the variable x_i (here β).

$$P(\beta; p, h) = \frac{1}{\sqrt{2\pi}\sigma_\beta(p, h)} \exp \left\{ -\frac{1}{2} \left(\frac{\beta - \mu_\beta(p, h)}{\sigma_\beta(p, h)} \right)^2 \right\} \quad (4.8)$$

The identity is assigned by choosing the particle hypothesis h which maximizes the likelihood ratio.

$$\frac{\mathcal{L}_h}{\mathcal{L}_\pi + \mathcal{L}_K + \mathcal{L}_p} \quad (4.9)$$

Using this method, every positive track is assigned a particle identification. However, at times the likelihood value is quite small when compared with the maximum likelihood for that species. This is the case for positrons which are classified by this method as positive pions, because they are the closest particle for which a hypothesis has been provided. To avoid these situations, the confidence level α of each track is calculated and a cut is applied on the minimum confidence. This cut can be easily varied to see how it changes the analysis result.

$$\alpha = 1 - \int_{\mu - \beta_{obs}}^{\mu + \beta_{obs}} P(\beta; p, h) d\beta \quad (4.10)$$

This quantity represents the probability to observe a value of β as far or farther from the mean as β_{obs} . Confidence levels close to zero correspond to tracks which are poorly identified as the class h . In the case that the PDF is Gaussian, the standard 1, 2, and 3 σ cuts on β vs. p can be understood simply as confidence levels of approximately 0.32 = 1-0.68, 0.05 = 1-0.95, and 0.01 = 1-0.99.

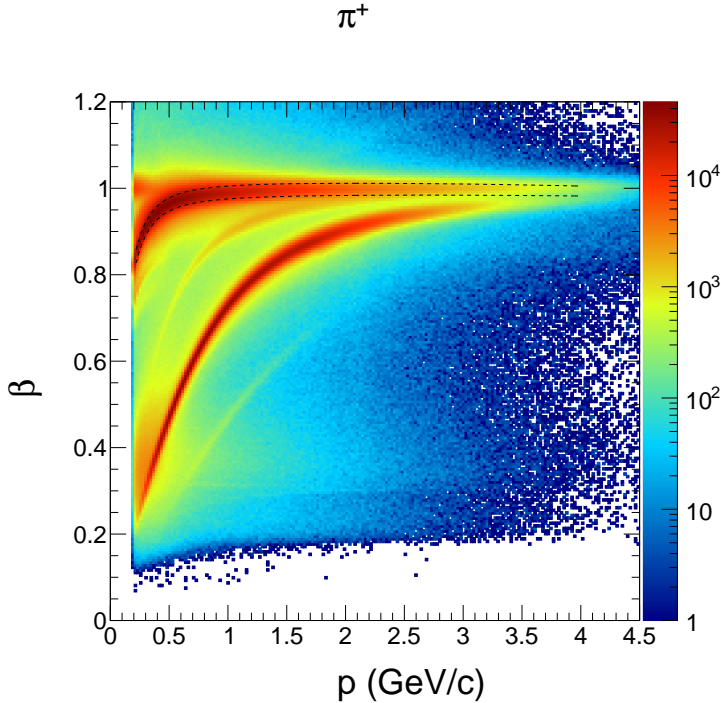


Figure 4.11: Shown above: All positive tracks overlaid with our determination of $\mu(p) \pm \sigma(p)$ for π^+

Determination of probability density functions for likelihood method

The most important and most difficult part of constructing the likelihood ratio identification is the determination of the mean and standard deviation of the probability density function (which depends on momentum) for the different hypotheses. In the case where exceptionally accurate monte carlo (MC) simulations of the detector are available, one can use the truth information and track matching to construct the β vs. p 2-dimensional histograms, and fit the $\mu(p)$ and $\sigma(p)$. In the absence of high quality MC, analysts typically fit directly the spectrum of β vs. p and extract the mean and variance. In this work, an enhanced sample of candidates for each of the three positive particles in question is created before doing the fitting. In this way, we hope that our fit better represents the true μ and σ for each particle. For fitting of pion and proton resolutions, positive tracks are assumed to be pions and the missing mass of the event is calculated. Then, a cut is placed around the neutron mass. In doing so, two main exclusive reactions are selected. The first is $ep \rightarrow e\pi^+N$, and the second is $ep \rightarrow ep\pi^0$. In this way most positrons, and positive kaons are removed from the sample prior to fitting. The mean and variance are fit using a third order polynomial in p (MINUIT χ^2 minimization is used). Negative pions and kaons are fit directly (as is normally done).

The parametrization used for the mean $\mu(p, h)$ and resolutions $\sigma(p, h)$ are shown below.

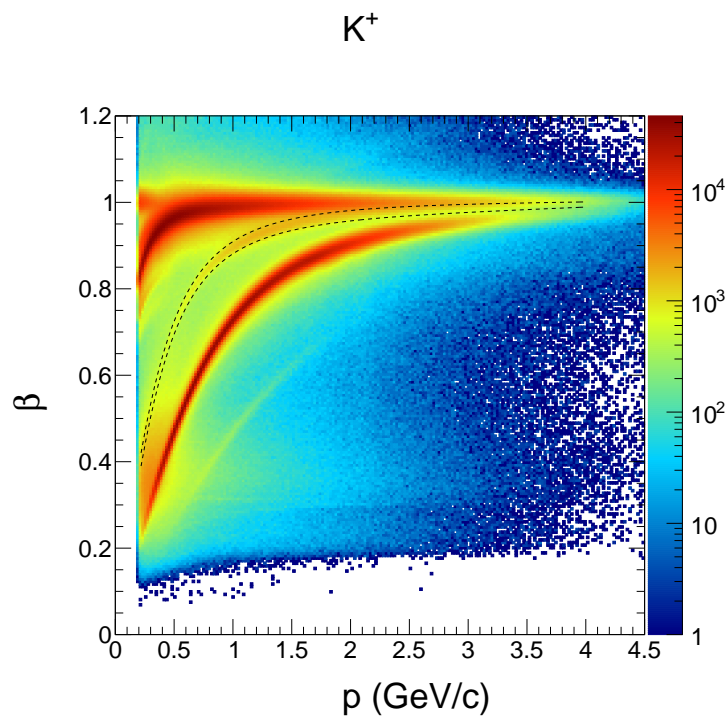


Figure 4.12: Shown above: All positive tracks overlaid with our determination of $\mu(p) \pm \sigma(p)$ for K^+

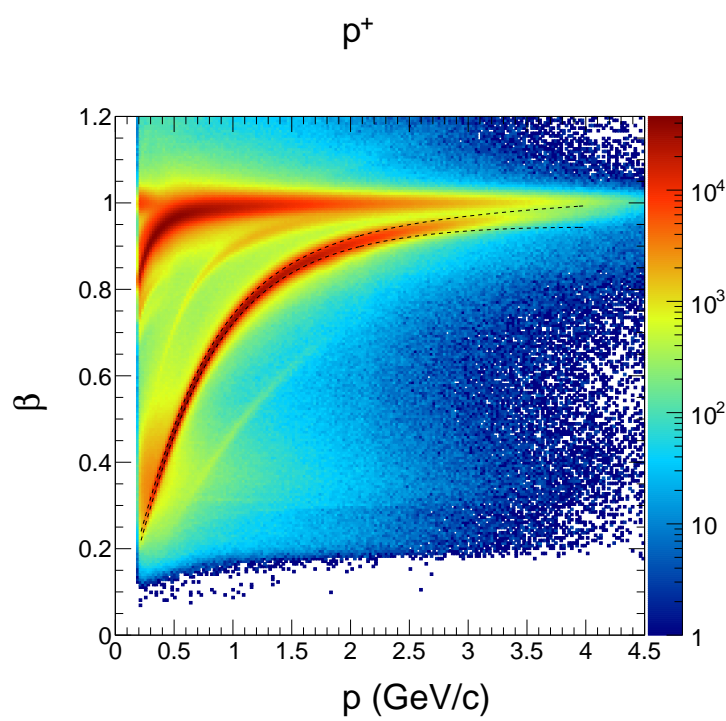


Figure 4.13: Shown above: All positive tracks overlaid with our determination of $\mu(p) \pm \sigma(p)$ for p^+

$$\mu(p, h) = \mu_{theory} + \Delta\mu \quad (4.11)$$

$$\mu_{theory} = \frac{1}{\sqrt{1 + (m_h/p)^2}} \quad (4.12)$$

$$\Delta\mu = \mu_0 + \mu_1 p + \mu_2 p^2 \quad (4.13)$$

$$\sigma(p, h) = \sigma_0 + \sigma_1 p + \sigma_2 p^2 \quad (4.14)$$

The values are displayed in the table below.

Hadron	Parameter	Sector 1	Sector 2	Sector 3	Sector 4	Sector 5	Sector 6
K^+	μ_2	0.00111554	-8.97687e-05	4.78796e-05	0.000376425	-0.00204856	0.000652209
K^+	μ_1	-0.00468038	6.19414e-05	-0.00081741	-0.00107931	0.00629181	-0.00264143
K^+	μ_0	0.00361012	0.00134921	0.00299674	0.00220194	0.000117821	0.00162582
K^+	σ_2	-0.000331838	-0.00105807	-0.000712404	-0.000573934	-0.000259289	0.000508389
K^+	σ_1	-0.00105857	0.00236686	0.000509169	0.000163467	-0.00233617	-0.00461598
K^+	σ_0	0.0154964	0.0117702	0.0140748	0.0143761	0.0184055	0.0180945
π^+	μ_2	-0.000962041	-0.000300602	-0.000306326	-3.2245e-05	-0.00226511	-0.000330818
π^+	μ_1	0.00296349	0.0016512	0.0021962	0.00176045	0.00750862	0.00126443
π^+	μ_0	-0.00225794	-0.00047045	0.000370406	0.000435526	-0.000449409	-0.00131045
π^+	σ_2	-0.000127659	0.000691895	-0.000289961	0.000315041	-0.000936521	-0.000131269
π^+	σ_1	-0.000489092	-0.0033948	0.00196853	-0.00197841	0.00212778	-0.000339411
π^+	σ_0	0.0155195	0.0167998	0.0124066	0.0157476	0.0145571	0.0141728
p^+	μ_2	-0.00039358	-0.000701003	-0.000347651	0.0004854	-0.00121666	0.000563786
p^+	μ_1	-0.000295423	0.00170899	0.000794901	-0.000744446	0.00376887	-0.00353545
p^+	μ_0	0.00227353	0.00231676	0.00364672	0.00276859	0.00128827	0.00439605
p^+	σ_2	0.001429	0.00144256	0.00124456	0.00190709	0.00141039	0.0011516
p^+	σ_1	-0.0021472	-0.00262226	-0.00196308	-0.00385218	-0.00186708	-0.00186749
p^+	σ_0	0.0107541	0.0109091	0.0104381	0.0115449	0.0109969	0.0107759
π^-	μ_2	3.28823666e-04	-1.30673670e-05	-2.32502052e-04	-9.75619848e-04	-5.89834444e-04	5.27496718e-04
π^-	μ_1	-3.94924663e-03	-2.66028661e-03	-1.28565631e-03	9.09410075e-04	-2.01610684e-03	-4.42276918e-03
π^-	μ_0	9.48011169e-04	1.55078786e-03	1.43431985e-03	1.35056935e-03	4.59833580e-03	2.30751866e-03
π^-	σ_2	4.37635504e-04	4.38306224e-04	5.32057510e-04	3.36999845e-04	7.74135462e-04	1.36515196e-04
π^-	σ_1	-3.28011836e-03	-3.28456104e-03	-3.82847286e-03	-3.11749323e-03	-4.63110728e-03	-2.21229710e-03
π^-	σ_0	1.63296567e-02	1.62229164e-02	1.59769911e-02	1.58803427e-02	1.74670064e-02	1.51753145e-02
K^-	μ_2	-2.72020947e-03	-5.21081786e-03	-2.13868763e-02	-4.45600034e-03	-7.60703841e-03	-5.27074813e-03
K^-	μ_1	1.78610401e-02	2.30787460e-02	9.49357818e-02	1.95764575e-02	3.63245785e-02	2.92417500e-02
K^-	μ_0	-2.26190100e-02	-2.22562379e-02	-1.02704771e-01	-2.25931014e-02	-5.10484618e-02	-3.19918187e-02
K^-	σ_2	1.76905114e-02	1.62989708e-02	3.60928130e-02	1.51270521e-02	1.91308107e-02	2.38470033e-02
K^-	σ_1	-7.74901862e-02	-7.33041628e-02	-1.57454534e-01	-7.26870393e-02	-9.23654247e-02	-1.02397836e-01
K^-	σ_0	1.07082820e-01	1.00573410e-01	1.93148260e-01	1.00993689e-01	1.26963814e-01	1.30057621e-01

Table 4.4: Values used to calculate the mean and resolutions for hadron likelihood based identification.

Chapter 5

Beam Spin Asymmetry Analysis

5.1 Introduction

Measurement of the beam spin asymmetry is carried out for the positively charged k-meson. As discussed in the introduction, the beam spin asymmetry theoretically depends on $F_{UU,L}$, $F_{UU,T}$, $F_{UU}^{\cos\phi}$, $F_{UU}^{\cos 2\phi}$, and $F_{LU}^{\sin\phi}$. By dividing the electron-kaon events into several bins of SIDIS kinematic variables, beam spin asymmetry measurements can be taken at different average values of the kinematic variables. Finally, the structure function ratios $A_{LU}^{\sin\phi}$, $A_{UU}^{\cos\phi}$, and $A_{UU}^{\cos 2\phi}$ can be extracted from each bin. In this chapter a discussion is provided of SIDIS event selection, the binning used in this analysis, measurement values with associated systematic uncertainties, and the extraction of structure function ratios using the ϕ dependence in each kinematic bin.

5.2 Event Selection and Binning

Event Selection

After particle identification, those events which have a trigger electron and a positive kaon are kept for analysis. Events are discarded that do not have $W > 2$ and $Q^2 > 1$, because they are not considered part of the deeply inelastic region. Additionally, to avoid exclusive resonances in the $ep \rightarrow eK^+X$ spectrum, a minimum value is imposed on the missing mass of the final state M_X ($ep \rightarrow eK^+X$). Here, we use $M_X(ep \rightarrow eK^+X) > 1.25$. Finally, a cut is applied to exclude low values of z_h to constrain our kinematics to the current factorization region where TMD factorization has been demonstrated at leading order. It is additionally required that $z_h < 0.75$ to avoid exclusive events. This restriction on z_h is not applied to the z_h axis, where we measure across the entire experimentally observed range.

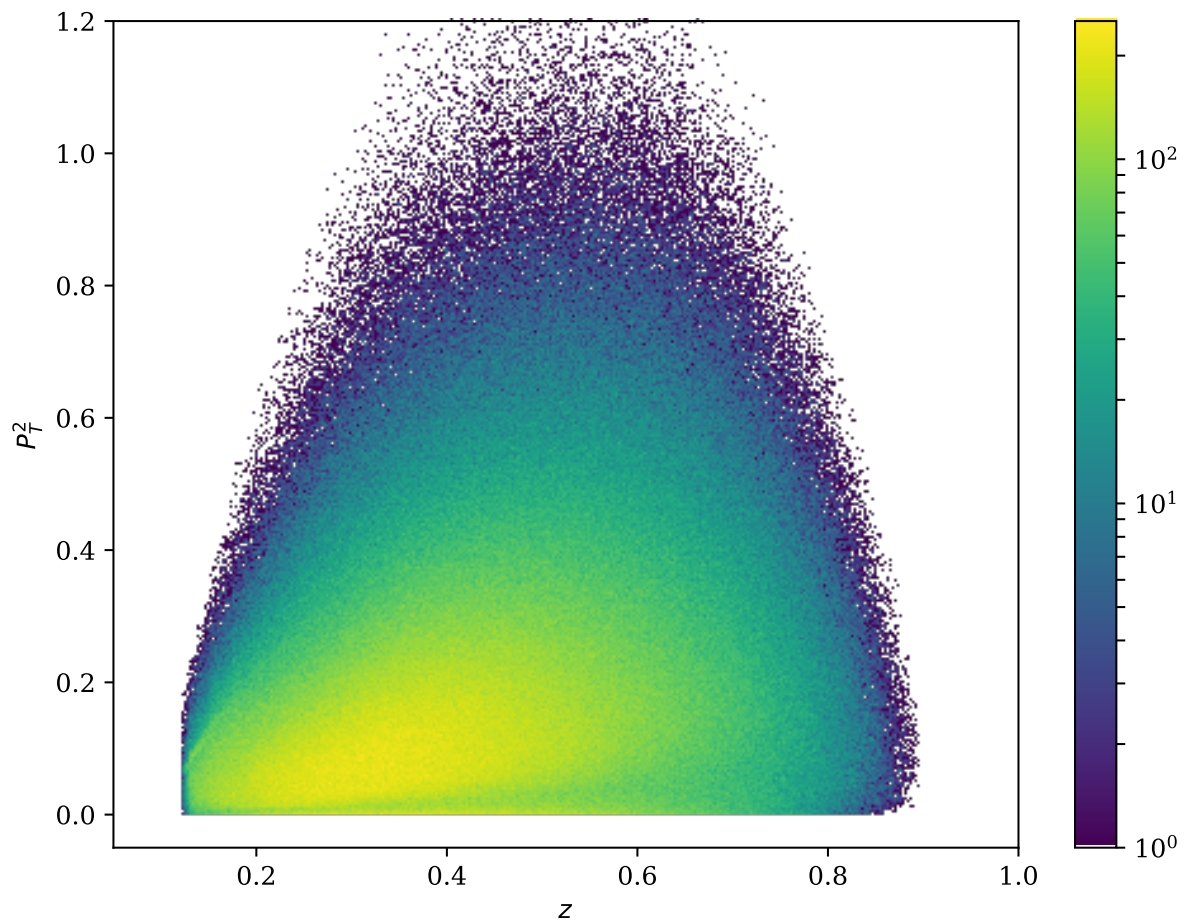


Figure 5.1: Correlation between z_h and P_T^2 for each event in our analysis sample.

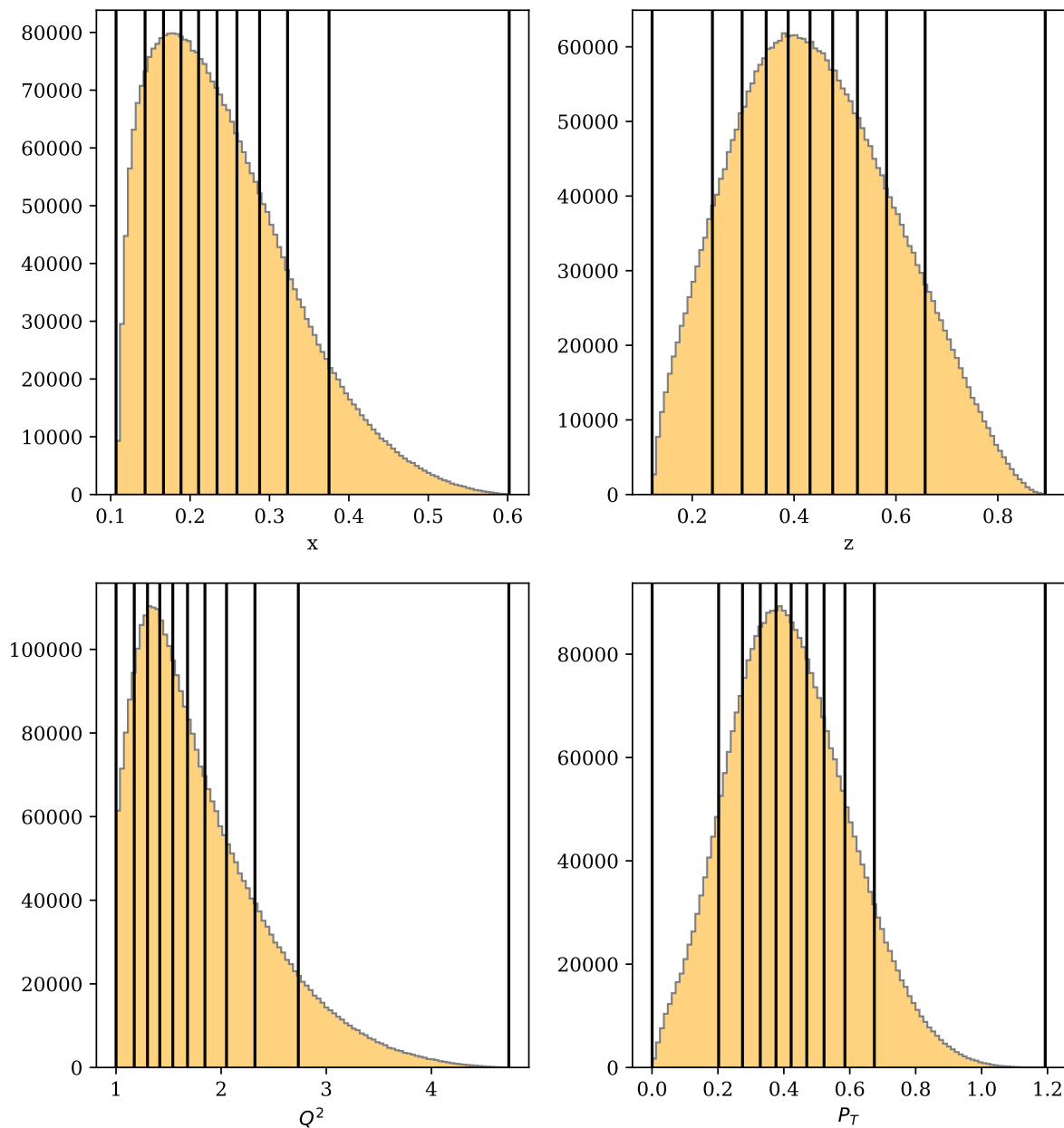


Figure 5.2: The binning used for each of the kinematic axes.

Binning

The beam spin asymmetry measurement is performed for the kinematic variables x , Q^2 , z_h , and P_T . For each variable 10 bins are chosen, as well as 12 bins in ϕ for a total of 120 analysis bins.

Bins were chosen using a simple method to ensure equal statistics in each bin. The procedure is described using the axis x as an example. First, all events are sorted by their x value from smallest to largest. Then, the smallest and largest values are recorded, which are x_1 and x_N if there are N events in the sample. Next, the target number of bins M is chosen (this choice depends on each analysis). Finally, the limits of each bin can be chosen by calculating the number of events per bin N/M and then using the value of x which corresponds to multiples of N/M in the sample.

$$\vec{b} = (x_1, x_{N/M}, x_{2N/M}, \dots, x_N) \quad (5.1)$$

Here, the symbol \vec{b} denotes a vector of $(M+1)$ x values which represent bin limits. The binning in ϕ is chosen to be regularly spaced between -180 and 180 degrees.

5.3 ϕ_h Distributions

Measured Asymmetry Values

In each bin i the beam spin asymmetry (here A_i) is calculated according to,

$$A_i = \frac{1}{P_e} \frac{n_+^i - n_-^i}{n_+^i + n_-^i} \quad (5.2)$$

where P_e is the average beam polarization over the dataset (74.9%). The symbols n_\pm^i refer to the number of events counted in bin i with helicity \pm .

Statistical Uncertainties

The uncertainty on the measured value of A_i can be attributed to statistical uncertainty on the counts n_i^\pm , and the uncertainty associated with the measurement of P_e . The statistical uncertainty reported on the measurement includes the contribution from counts, but not from the uncertainty in P_e which is included in the systematic errors. In general, the uncertainty in a measured observable \mathcal{O} depends on the uncertainty of the parameters (here denoted by $\vec{\theta}$) used to construct it $\vec{\theta}$ in the following way (see appendix for derivation).

$$\sigma_{\mathcal{O}}^2 = \sum_{i=1}^N \sum_{j=1}^N \frac{\partial \mathcal{O}}{\partial \theta_i} \frac{\partial \mathcal{O}}{\partial \theta_j} \rho_{ij} \sigma_i \sigma_j \quad (5.3)$$

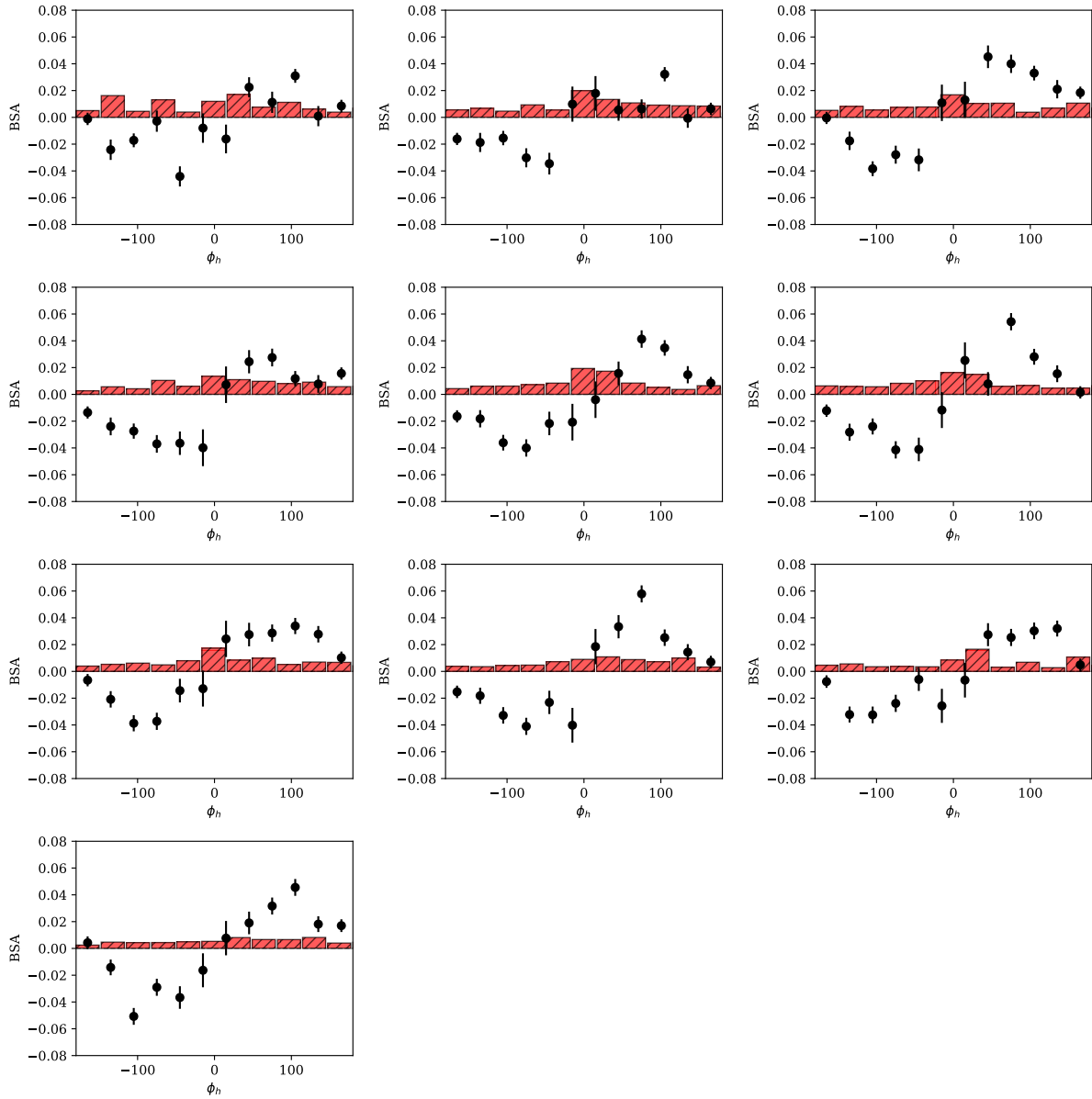


Figure 5.3: The ϕ_h dependence is shown for each bin of x , increasing in value from the top left to the bottom right. The statistical uncertainty is shown as black error bars on each point. The total systematic uncertainty is shown as a red bar centered at zero.

For the beam spin asymmetry in the i^{th} bin A_i one finds that without correlations ($\rho_{ij} = \delta_{ij}$) the error propagation proceeds as shown below.

$$\sigma_A^2 = \frac{A^2}{P_e^2} \sigma_{P_e}^2 + \frac{4(n_-^2 \sigma_+^2 + n_+^2 \sigma_-^2)}{P_e^2 (n_+ + n_-)^4} \quad (5.4)$$

The first term which is the contribution from the variance in the measurements of beam polarization will be included as a systematic error. The second term is used as the statistical error bars shown through the analysis. The counts n_{\pm}^i for the i^{th} bin are assumed to be Poisson in nature, and therefore have a variance equal to the expected number of counts $\sigma_{\pm}^2 = n_{\pm}^i$. With this expression for the statistical uncertainty on the counts, and dropping the beam polarization term for now, the expression becomes:

$$\sigma_A^2 = \frac{4n_+ n_-}{P_e^2 (n_+ + n_-)^3} \quad (5.5)$$

Systematic Uncertainties

Systematic effects are shifts or biases in the measured result of some observable as a result of the procedure used in the measurement. Systematic effects can typically be identified and corrected for, or removed all together from the measurement. In the cases where an effect cannot be completely removed, the degree to which the correction for the effect is uncertain is included in the result of the measurement as a systematic uncertainty [19].

Sources of systematic effects can include background events from different processes which enter the sample, calibrations of different detector systems, misalignment in detector geometry, and biases in selection criteria. Each of the systematic sources mentioned here has at least one associated procedure for correcting it's effect on the analysis. As an example consider momentum corrections in CLAS. These corrections are performed to remove the effect of slight misalignment in detector geometry from what is in reconstruction, as well as slight differences between the true magnetic field and the field map used in reconstruction. These physical effects introduce a systematic effect, the particle 4-momenta reconstructed are shifted away from the true values. Standard reactions (elastic scattering) can be used to develop corrections for the 4-momenta of particles, and these corrections typically depend on a set of parameters $\vec{\theta}$, which have an associated parameter uncertainty described by a covariance matrix V_{ij} . It is these parameter uncertainties that propagate through to the final observables, and the assignment of the magnitude of such effects is then what is referred to as systematic uncertainty.

Systematic uncertainties are included using the standard equation for error propagation. In some cases it is possible to analytically find the derivatives needed to calculate the dependence of the ob-

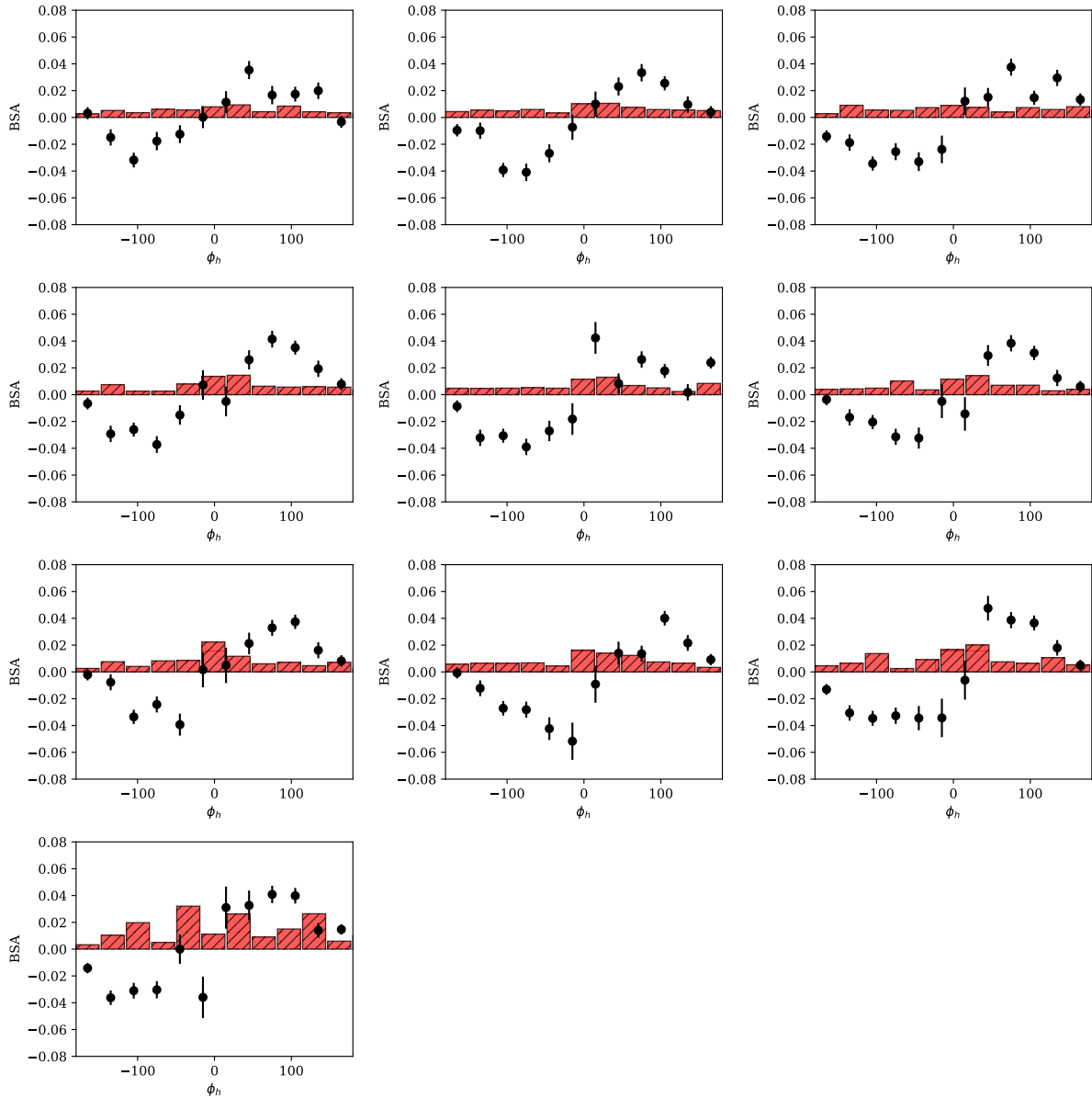


Figure 5.4: The ϕ_h dependence is shown for each bin of z_h , increasing in value from the top left to the bottom right. The statistical uncertainty is shown as black error bars on each point. The total systematic uncertainty is shown as a red bar centered at zero.

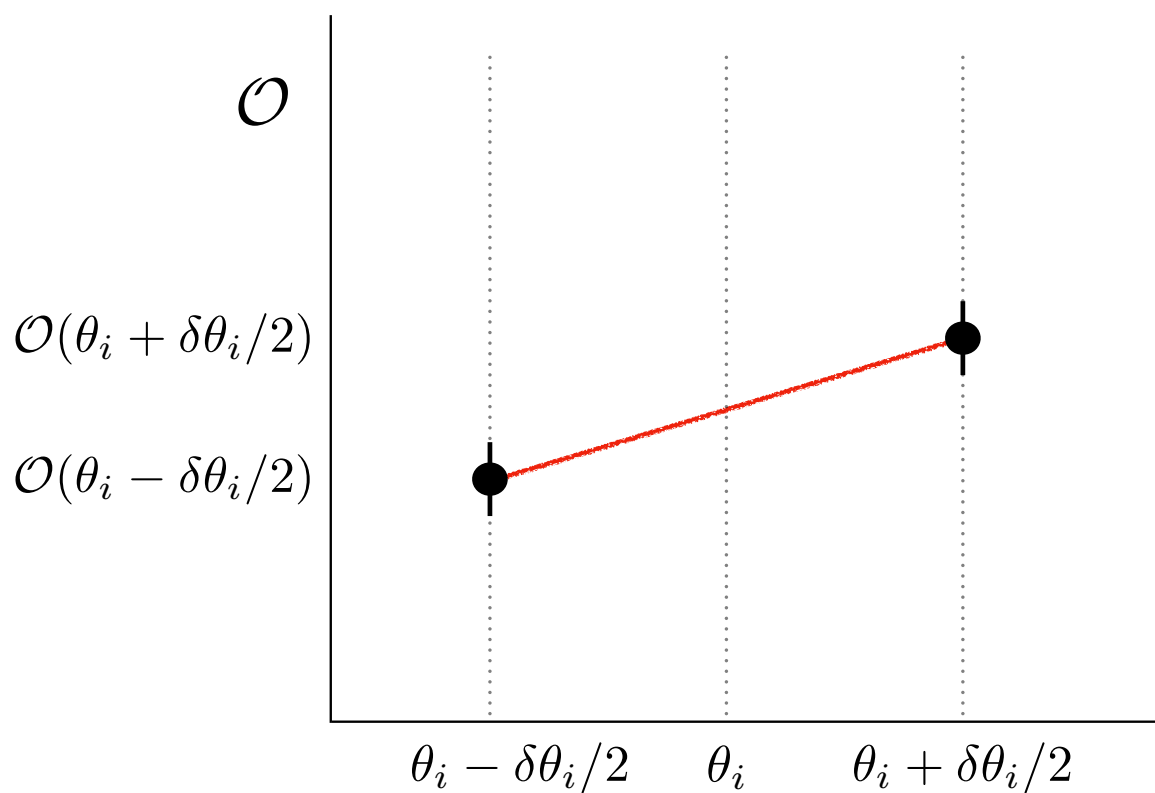


Figure 5.5: The analysis is run for variations in the input parameters θ_i to calculate the dependence of the result \mathcal{O} on each parameter, as described in this section.

servable on a source of systematic uncertainty. This is the case for effect of the variance of the beam polarization on the beam spin asymmetry observable. However in many cases, it is not possible to analytically calculate the effect of an analysis parameter θ_i on the observable \mathcal{O} . Since the observable is usually calculated using some computational chain which starts with the input parameters $\vec{\theta}$, it is possible to find the dependence of the observable \mathcal{O} on the inputs numerically.

$$\frac{\partial \mathcal{O}}{\partial \theta_i} \approx \frac{\mathcal{O}(\theta_i + \sigma_{\theta_i}/2) - \mathcal{O}(\theta_i - \sigma_{\theta_i}/2)}{\sigma_{\theta_i}} \quad (5.6)$$

After inserting the above into equation 5.3 one finds,

$$\sigma_{\mathcal{O}}^2 = \sum_{i=1}^n \sum_{j=1}^n \rho_{ij} (\mathcal{O}(\theta_i + \sigma_{\theta_i}/2) - \mathcal{O}(\theta_i - \sigma_{\theta_i}/2)) (\mathcal{O}(\theta_j + \sigma_{\theta_j}/2) - \mathcal{O}(\theta_j - \sigma_{\theta_j}/2)) \quad (5.7)$$

where ρ_{ij} is the correlation $V_{ij}/\sigma_i \sigma_j$. In most cases, these correlations are assumed to be zero. In some cases, when the parameters θ_i, θ_j come from a fit one may have a correlation provided by the covariance matrix and it should be used. In the case where correlations are assumed to be zero, the total systematic uncertainty is simply the quadrature sum of the shift in the observable within the uncertainty window on each parameter.

$$\sigma_{\mathcal{O}}^2 = \sum_{i=1}^n \left[\mathcal{O}(\theta_i + \sigma_{\theta_i}/2) - \mathcal{O}(\theta_i - \sigma_{\theta_i}/2) \right]^2 \quad (5.8)$$

Another approach exists that takes into account possible correlations between the analysis parameters θ_i . The approach consists of generating M sets of parameters $\vec{\theta}$ and obtaining M results for the observable \mathcal{O} . The results are then interpreted statistically and the observable value and total systematic error are reported as the mean and standard deviation of the results. This Monte Carlo based technique has the advantage that it is conceptually simple, and allows the capture of correlations. However, it can be computationally intensive to perform the analysis hundreds of times. Additionally, only using this technique without first testing the individual size of each systematic source removes the possibility of correcting for or removing biases.

$$\langle \mathcal{O} \rangle = \frac{1}{M} \sum_{i=1}^M \mathcal{O}_i \quad (5.9)$$

$$\sigma_{\mathcal{O}}^2 = \frac{1}{M-1} \sum_{i=1}^M (\mathcal{O}_i - \langle \mathcal{O} \rangle)^2 \quad (5.10)$$

Sources of Systematic Uncertainty

Table 5.1 below summarizes the sources of systematic uncertainty considered in this analysis.

Except for the beam polarization and the momentum of the kaon track, all parameters listed in the

Source	Variation	Magnitude
Beam polarization	0.024	0.000672
DC Region 1 Fid.	1 (cm)	0.001344
DC Region 3 Fid.	3 (cm)	0.001821
EC-W	12 (cm)	0.000948
EC-V	12 (cm)	0.000797
EC-U	12 (cm)	0.002487
Kaon Confidence (α)	0.01-0.07	0.001827
θ_{cc} Matching	σ	0.001152
EC Energy Deposition	0.01 (GeV)	0.001644
p_{K^+}	$2.5-E_{beam}$	0.002360
EC Sampling Fraction	0.5σ	0.001240
Z-Vertex	0.5 (cm)	0.002581
Statistical	-	0.007494
MC Estimate	-	0.002917

Table 5.1: Different sources of systematic effect considered in this analysis. The magnitude of the effect is shown here averaged over all bins. The units of the shift are just the same units of the asymmetry value.

table are treated using the formalism outlined above. The beam polarization uncertainty quoted at 2.4% contains contributions from the standard deviation of the Moller polarimetry measurements (0.2%), residual target polarization effects (1.4%), and atomic motion/finite acceptance corrections (0.8%).

Because of the inability to distinguish kaon, pion, and proton tracks at higher momentum, the maximum kaon track momentum is varied between 5.5 (no maximum) and 2.5 GeV. The difference between these results is quoted as a systematic uncertainty and added in quadrature with the other sources. This source of systematic uncertainty has a larger effect on the z_h -axis, because z_{max} is limited by limiting p_{max} . While for the large z_h -bins this contribution is dominant, its size is comparable with other systematic sources throughout the remainder of the bins.

5.4 Extraction of Modulations

The motivation to measure the beam spin asymmetry in several kinematic bins as well as bins of ϕ_h is to perform an estimate of the value of structure functions at the kinematic points (more precisely the average value of the structure functions over the range of values included in a point). To do this, the authors perform parameter estimation on the ϕ_h distributions taking as a model the theoretical dependence of the beam spin asymmetry on ϕ_h .

$$f(\phi_h, \vec{a}) = \frac{a_0 \sin \phi_h}{1 + a_1 \cos \phi_h + a_2 \cos(2\phi_h)} \quad (5.11)$$

The parameters \vec{a} are the structure function ratios to be extracted. The simplest way to extract these parameters is to use χ^2 minimization implemented in a standard fitting package. In these approaches, χ^2 is defined as the square difference between the observed data values and those predicted by the

model, normalized by the error. If the fluctuation between the data and theory predictions is on the order of the error, the χ^2 is simply on the order of the number of data points. The parameters \vec{a} which best describe the data are those which make the $\chi^2(\vec{a})$ assume its minimum value. This minimization is done in practice with gradient descent or quasi-Newton's method based algorithms like those provided in `Minuit` or `scipy.optimize.minimize`, the details of such algorithms will not be discussed here. It is sufficient to say that these minimization methods produce the parameters \vec{a} , and an estimate of the covariance matrix V . The parameters and their errors become the extracted value and uncertainty of the structure function ratio in each bin.

Unfortunately, applying the standard single-fit procedure described above does not always produce stable results. In some cases, the resulting parameter sets are reasonable, in other cases however the parameters in the denominator become nonphysically large and oppose each other. This effect has motivated previous analysts to search for other means of extracting the dominant $\sin \phi_h$ behavior from the distributions. One common technique is to assume that a_1 and a_2 of above are small compared to 1. The analyst can then fit the ϕ_h distribution with just one linear parameter a_0 . This produces a stable result, but has the disadvantage that one needs to introduce a systematic uncertainty associated with the difference observed between using the full model (with a restricted range for the parameters in the denominator) and the results obtained using the single parameter model. Additionally, the structure function decomposition of the SIDIS cross section relies on theoretically solid ground, therefore it should be used in its full form. If the data contain little information regarding the structure function ratios in the denominator, the authors believe it more valuable to demonstrate this by extracting those parameters with (large) errors, rather than ignore their contribution. In order to accomplish this, the method of replicas (or parametric bootstrapping) is used to perform the parameter extraction. The replica method consists of generating N_{rep} pseudo-data ϕ_h distributions which have a normal distribution located at the observed value, and with a variance equal to the statistical errors on the associated data point.

$$\vec{A}_{rep} = \mathcal{N}(\vec{A}, \sigma_A) \quad (5.12)$$

Where here \vec{A} is a vector of length n_{phi} bins, representing the measured beam spin asymmetry for each value of ϕ_h in a given kinematic bin. Each of these distributions is fit with the full model, and the resulting parameter values are saved. The final reported value for each fit parameter, as well as its uncertainty can be reported as the mean, and standard deviation of the fit results. This procedure which is similar to bootstrapping, can be seen as an attempt to fit the underlying distribution that generated the data while avoiding the statistical noise. This technique has been discussed in [20].

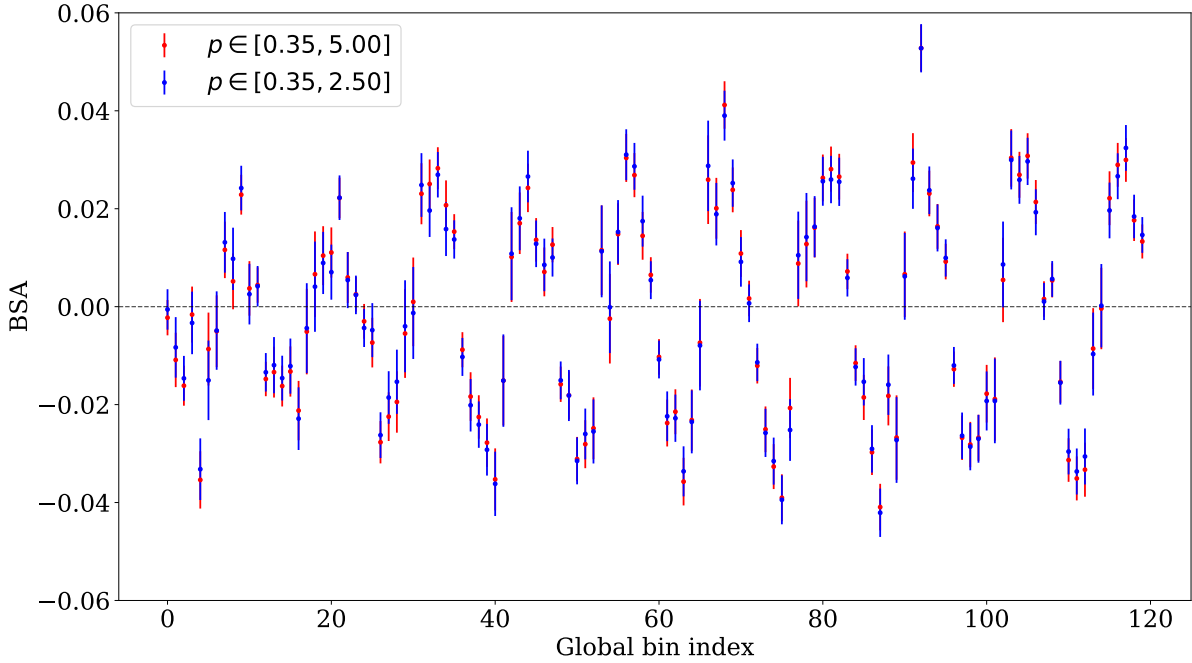


Figure 5.6: The BSA for each bin of x, ϕ_h (all plotted together on the x-axis) is compared with and without a maximum momentum (no tracks exceed 5 GeV) for the kaon track. The global bin coordinate on the x-axis is $i + n_\phi * j$ where i is the ϕ_h bin, j is the x bin, and n_ϕ is the number of ϕ bins (12). Both i and j start at 0.

$$\langle a_j \rangle = \sum_{i=1}^{N_{rep}} a_j^{(i)} \quad (5.13)$$

$$\sigma_{a_j}^2 = \frac{1}{N_{rep} - 1} \sum_{i=1}^{N_{rep}} (a_j^{(i)} - \langle a_j \rangle)^2 \quad (5.14)$$

Results

As is the case for positive pions, the observed structure function ratio $A_{LU}^{\sin \phi}$ is positive for all kinematic points that were measured. In general, this extraction reveals that the $\sin \phi_h$ moment has a magnitude around 3% for most kinematic points, and depends weakly on the kinematic variables used in this analysis. The relative asymmetry value to total error ratio is around 1.5 for most measured points.

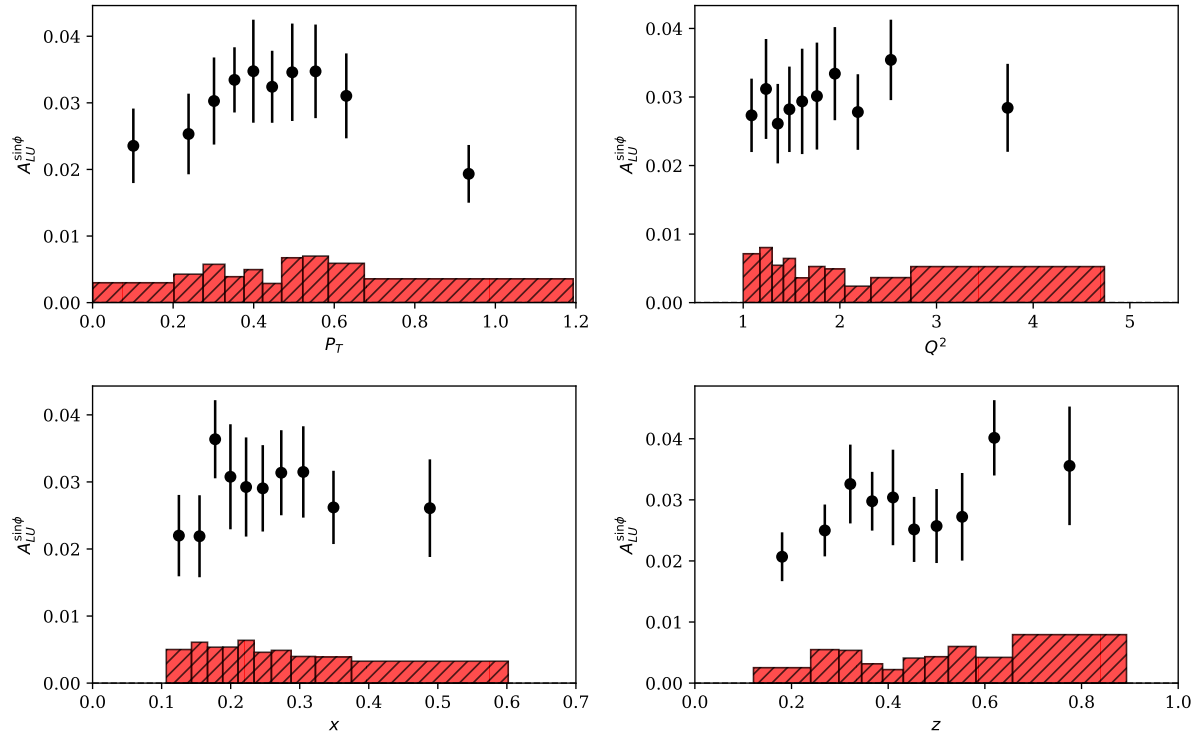


Figure 5.7: Our extraction of $A_{LU}^{\sin\phi}$ for the kinematic bins described above. The black error bars represent uncertainty in the extraction of the parameter value. Red error bars are systematic uncertainties.

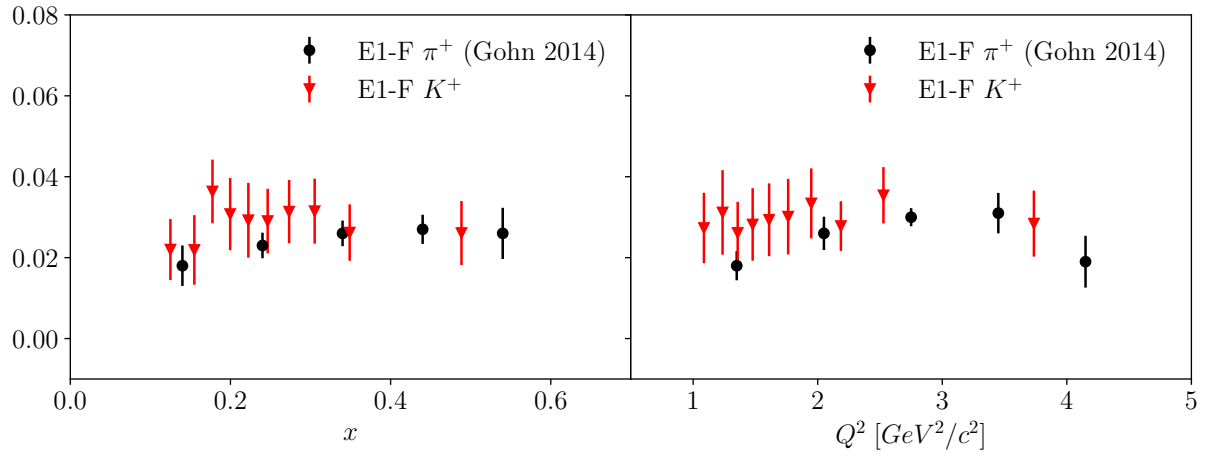


Figure 5.8: In this figure the results of this study for positively charged kaons are compared with previous results from the same dataset produced by [8] for positively charged pions. This figure shows the x and Q^2 dependence of $A_{LU}^{\sin\phi_h}$.

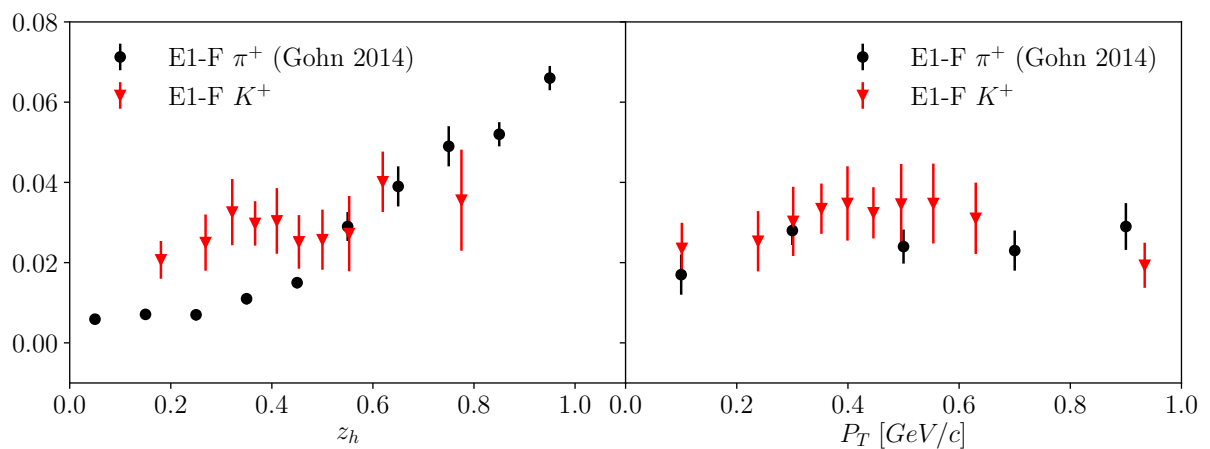


Figure 5.9: In this figure the results of this study for positively charged kaons are compared with previous results from the same dataset produced by [8] for positively charged pions. This figure shows the z_h and P_T dependence of $A_{LU}^{\sin \phi_h}$.

Appendix A: Derivation of formulas related to errors

Propagation of errors

Let \vec{x} be a set of n random variables $\vec{x} = (x_1, x_2, \dots, x_n)$ and known mean $\mu_i = \langle x_i \rangle$ and covariance $V_{ij} = \langle x_i x_j \rangle - \langle x_i \rangle \langle x_j \rangle$. Suppose that we measure a function $f(\vec{x})$ that depends on the variables \vec{x} and we want to understand how the covariances V_{ij} on \vec{x} will show up manifest themselves as errors on our measurement of $f(\vec{x})$. We can start by expanding our function around the expected value of x_i .

$$f(\vec{x}) \approx f(\vec{\mu}) + \sum_{i=1}^n \frac{\partial f}{\partial x_i} \Big|_{x_i=\mu_i} (x_i - \mu_i) \quad (15)$$

We can then take the expectation value of our function.

$$\langle f(\vec{x}) \rangle = \langle f(\vec{\mu}) \rangle + \sum_{i=1}^n \frac{\partial f}{\partial x_i} \Big|_{x_i=\mu_i} \langle x_i - \mu_i \rangle \quad (16)$$

Where here the term $\langle x_i - \mu_i \rangle$ is zero.

$$\langle x_i - \mu_i \rangle = \langle x_i \rangle - \mu_i = \mu_i - \mu_i = 0 \quad (17)$$

It is apparent then that the expectation value of our function f evaluated close to the expected values of our variables \vec{x} is just the function evaluated at the expectation value of the random variables \vec{x} .

$$\langle f(\vec{x}) \rangle = \langle f(\mu) \rangle = f(\mu) \quad (18)$$

We can also consider the second moment $\langle f^2(\vec{x}) \rangle$,

$$\langle f^2(\vec{x}) \rangle \approx \left\langle \left(f(\vec{\mu}) + \sum_{i=1}^n \frac{\partial f}{\partial x_i} \Big|_{x_i=\mu_i} (x_i - \mu_i) \right)^2 \right\rangle \quad (19)$$

which is,

$$= \langle f^2(\mu) \rangle + \sum_{i=1}^n \sum_{j=1}^n \frac{\partial f}{\partial x_i} \Big|_{x_i=\mu_i} \frac{\partial f}{\partial x_j} \Big|_{x_j=\mu_j} \langle (x_i - \mu_i)(x_j - \mu_j) \rangle + 2 \left\langle f(\mu) \sum_{i=1}^n \frac{\partial f}{\partial x_i} \Big|_{x_i=\mu_i} (x_i - \mu_i) \right\rangle \quad (20)$$

and the last expectation value vanishes due to the same logic used when calculating the first moment. We recognize the term $\langle (x_i - \mu_i)(x_j - \mu_j) \rangle$ as the element of the covariance matrix V_{ij} . Our second moment is then complete as follows.

$$\langle f^2(\vec{x}) \rangle = f^2(\mu) + \sum_{i=1}^n \sum_{j=1}^n \frac{\partial f}{\partial x_i} \Big|_{x_i=\mu_i} \frac{\partial f}{\partial x_j} \Big|_{x_j=\mu_i} V_{ij} \quad (21)$$

We can then calculate the variance of the function.

$$\sigma_f^2 = \langle f^2(\vec{x}) \rangle - \langle f(\vec{x}) \rangle^2 \quad (22)$$

$$= (f^2(\vec{\mu}) - f^2(\vec{\mu})) + \sum_{i=1}^n \sum_{j=1}^n \frac{\partial f}{\partial x_i} \Big|_{x_i=\mu_i} \frac{\partial f}{\partial x_j} \Big|_{x_j=\mu_i} V_{ij} \quad (23)$$

$$= \sum_{i=1}^n \sum_{j=1}^n \frac{\partial f}{\partial x_i} \Big|_{x_i=\mu_i} \frac{\partial f}{\partial x_j} \Big|_{x_j=\mu_i} V_{ij} \quad (24)$$

This is the standard error propagation formula which is widely used. These correlations σ_{ij} can arise from several sources.

- Common measurement uncertainties.
- Correlations in $x_i x_j$ leading to correlations in $\sigma_i \sigma_j$.

References

- [1] E. Leader and M. Anselmino, *Proceedings, 8th International Symposium on High-energy Spin Physics: Minneapolis, Minnesota, USA, September 12-17, 1988. Vol. 1, 2*, Z. Phys. **C41**, 239 (1988), [AIP Conf. Proc.187,764(2008)].
- [2] P. J. Mulders and R. D. Tangerman, Nucl. Phys. **B461**, 197 (1996), [Erratum: Nucl. Phys.B484,538(1997)], arXiv:hep-ph/9510301 [hep-ph].
- [3] A. Bacchetta, M. Diehl, K. Goeke, A. Metz, P. J. Mulders, and M. Schlegel, JHEP **02**, 093 (2007), arXiv:hep-ph/0611265 [hep-ph].
- [4] A. Airapetian *et al.* (HERMES), Phys. Rev. Lett. **103**, 152002 (2009), arXiv:0906.3918 [hep-ex].
- [5] A. Airapetian *et al.* (HERMES), Phys. Rev. **D87**, 074029 (2013), arXiv:1212.5407 [hep-ex].
- [6] M. Aghasyan *et al.* (COMPASS), Phys. Rev. **D97**, 032006 (2018), arXiv:1709.07374 [hep-ex].
- [7] M. Anselmino, M. Boglione, U. D'Alesio, J. O. Gonzalez Hernandez, S. Melis, F. Murgia, and A. Prokudin, Phys. Rev. **D92**, 114023 (2015), arXiv:1510.05389 [hep-ph].
- [8] W. Gohn *et al.* (CLAS), Phys. Rev. **D89**, 072011 (2014), arXiv:1402.4097 [hep-ex].
- [9] Y. X. Zhao *et al.* (Jefferson Lab Hall A), Phys. Rev. **C90**, 055201 (2014), arXiv:1404.7204 [nucl-ex].
- [10] C. W. Leemann *et al.*, Ann. Rev. Nucl. Part. Sci. **51**, 413 (2001).
- [11] Y. C. Chao *et al.*, J. Phys. Conf. Ser. **299**, 012015 (2011).
- [12] G. Adams *et al.*, Nucl. Instrum. Meth. **A465**, 414 (2001).
- [13] M. D. Mestayer *et al.*, Nucl. Instrum. Meth. **A449**, 81 (2000).
- [14] E. S. Smith *et al.*, Nucl. Instrum. Meth. **A432**, 265 (1999).
- [15] M. Amarian *et al.*, Nucl. Instrum. Meth. **A460**, 239 (2001).
- [16] N. A. Harrison, *Exploring the Structure of the Proton via Semi-Inclusive Pion Electroproduction*, Ph.D. thesis, Connecticut U. (2010).
- [17] M. Mirazita, "Kinematic corrections for e1-f," .
- [18] R.-G. Ping *et al.*, Int. J. Mod. Phys. **A24S1**, 23 (2009).

- [19] R. Barlow, in *Advanced Statistical Techniques in Particle Physics. Proceedings, Conference, Durham, UK, March 18-22, 2002* (2002) pp. 134–144, arXiv:hep-ex/0207026 [hep-ex].
- [20] G. Watt and R. S. Thorne, JHEP **08**, 052 (2012), arXiv:1205.4024 [hep-ph].